NASA TECHNICAL MEMORANDUM 102599

RELEVANCE OF IMPACTER SHAPE TO NONVISIBLE DAMAGE AND RESIDUAL TENSILE STRENGTH OF A THICK GRAPHITE/EPOXY LAMINATE

C. C. Poe, Jr.

January 1990

National Aeronautics and
Space Administration

Langley Research Center
Hampton, Virginia 23665

RELEVANCE OF IMPACTER SHAPE TO NONVISIBLE DAMAGE AND RESIDUAL TENSILE STRENGTH OF A THICK GRAPHITE/EPOXY LAMINATE

by C. C. Poe, Jr.

NASA Langley Research Center
Hampton, Virginia 23665

SUMMARY

A study was made to determine the relevance of impacter shape to nonvisible damage and tensile residual strength of graphite/epoxy cases for the solid rocket motors of the Space Shuttle. Impacters were dropped onto 30.5-cm- (12-in.) long rings (short cylinders) that were 76.2-cm (30-in.) in diameter and 36-mm- (1.4-in.) thick. The kinetic energies ranged from 17.0 to 136 J (12.5 to 100 ft-lbf). Some rings were filled with inert propellant and some were empty. A 5 kg (11 lbm) impacter was used with the following shapes: 12.7-mm- (0.5-in.) and 25.4-mm- (1.0-in.) diameter hemispheres, a sharp corner, and a 6.3-mm- (0.25-in.) diameter bolt-like rod. The rings were impacted numerous times around the circumference and cut into 51-mm- (2-in.) wide specimens. Impacts with the rod impacter were simulated by pressing the rod against the face of specimens. The specimens were uniaxially loaded to failure in tension. The investigation revealed that damage initiated when the contact pressure exceeded a critical level. However, the damage was not visible on the surface until an even higher pressure was exceeded. Thus, damage was not visible on the surface for a wide range of impact energies. The damage on the surface consisted of a crater shaped like the impacter, and the damage below the surface consisted of broken fibers. The impact energy to initiate damage or cause visible damage on the surface increased approximately with impacter diameter to the third power. The reduction in strength for nonvisible damage increased with increasing diameter, 9 and 30 percent for the 12.7-mm- (0.5-in.) and 25.4-mm- (1.0-in.) diameter hemispheres, respectively. The corner impacter made visible damage on the surface for even the smallest impact energy. The rod impacter acted like a punch and sliced through the composite. Even so, the critical level of pressure to initiate damage was the same for the rod and hemispherical impacters. Factors of safety for nonvisible damage increased with increasing kinetic energy of impact. The effects of impacter shape on impact force, damage size, damage visibility, and residual tensile strength were predicted quite well assuming Hertzian contact and using maximum stress criteria and a surface crack analysis.

INTRODUCTION

Recently, NASA developed several sets of solid rocket motors with graphite/epoxy cases to use in lieu of existing motors with steel cases for the Space Shuttle. These light-weight motor's were to have been used for certain missions that required a lower mass at launch. (The program was canceled before the first flight.) The cases were made using a wet filament-winding process, hence the name filament-wound case (FWC). It was desired, but not required, that the FWC's be reusable like the steel cases. Each light-weight motor would have consisted of four FWC's, a forward case, two center cases, and an aft case. The FWC's were 3.66 m (12 ft) in diameter and were joined together with steel pins. The forward and center FWC's were 7.6 m (25 ft) in length, and the aft FWC was somewhat shorter. The thickness of the membrane region away from the ends was approximately 36 mm (1.4 in.). The ends were thicker to withstand the concentrated pin loads. The FWC's are designed primarily for internal pressure caused by the burning propellant. However, the motors are subjected to bending when the main engines of the orbiter ignite, causing relatively large compression stresses in the aft FWC's. In fact, one FWC that contained a large area of high porosity or delaminations failed between limit and ultimate conditions during a structural test in which this bending condition was being simulated. The ultrasonic inspection could not distinguish between high porosity and delaminations.

For graphite/epoxy pressure vessels with thin walls, the reduction of burst pressure by impact damage is widely known. See, for example, [1]. However, because of the stoutness of the FWC's, it was not expected that low-velocity impacts by tools and equipment could seriously reduce strength. However, dropped tools and equipment are not the only threat; the potential for handling accidents is also significant. In fact one empty FWC was dropped in the factory during the development program. The FWC's were to have been manufactured and loaded with propellant in Utah and shipped by rail to Florida. Each of the longer FWC's had a mass of about 4,500 kg (10,000 lbm) empty and about 140,000 kg (300,000 lbm) when filled with propellant. The potential energy or kinetic energy of even an empty FWC when lifted 1 m (39 in.) would be over 44,000 J (33,000 ft-lbf). Thus, handling accidents can potentially cause more serious impact damage than dropped tools and equipment.

In a previous investigation conducted at Langley Research Center [2-5], the effect of low-velocity impacts on the tension strength of an FWC was determined for an impacter with a hemispherically shaped end having a 25.4-mm- (1.0-in.) diameter. (The compression failure in the bending test had not occurred at this time.) Impacters of various masses were dropped from various heights onto 36-mm- (1.4-in.) thick graphite/epoxy rings (short cylinders) to simulate falling tools and equipment. Impact energies ranged from 38 to 447 J (28 to 329 ft-lbf). The rings were impacted numerous times around the circumference and cut into specimens. Then, the specimens were loaded uniaxially in tension to failure. For impact energies of 38 J (28 ft-lbf) and greater, the laminate was damaged and the residual tensile strength was reduced accordingly. The damaged region contained broken fibers, the locus of which resembled cracks. Up to about 100 J (74 ft-lbf), the damage was not visible on the surface, but the tensile strength was reduced as much as 30 percent. Even for the largest energy 447 J (329 ft-lbf), the damage was localized and did not extend to the back face. The damage size (breadth and depth) and residual tensile strength were

predicted assuming Hertzian contact and using maximum stress criteria and surface crack analysis. However, the size and nature of the damage could not be positively determined nondestructively to verify the predictions of damage [6-9]. Thus, a number of specimens were damaged by simulated impacts and deplied [10]. The maximum size of the damaged region was in good agreement with that predicted by maximum stress criteria. The broken fibers appeared to have been caused by shear failure of the epoxy.

Because of concern about reduction in strength due to nonvisible impact damage, the present investigation was made to determine the relevance of impacter shape to nonvisible damage and the associated reduction in strength. Accordingly, impact tests were conducted with the following additional indenters: a 12.7-mm- (0.5-in.) diameter hemisphere, a sharp corner, and a 6.3-mm- (0.25-in.) diameter bolt-like rod. The hemisphere and corner indenters were attached to the end of a 5 kg (11.1 lbm) impacter and dropped from various heights onto 36-mm- (1.4-in.) thick graphite/epoxy rings (short cylinders). These rings were taken from the same cylinder as those in [2-9]. The rings were impacted numerous times around the circumference and cut into 51-mm- (2-in.) wide specimens as in the earlier investigation. Impacts with the rod indenter were simulated by pressing the rod against the face of specimens using a testing machine. The specimens were then loaded uniaxially in tension to failure. The effects of indenter shape on impact force, damage size, damage visibility, and residual tensile strength were predicted assuming Hertzian contact and using the maximum stress criteria and surface crack analysis reported in [3-5]. Factors of safety for strength reduction with nonvisible damage were calculated in terms of impact energy.

The material, test apparatus, and procedure were described in [2-4]. They will also be reviewed here for the convenience of the reader.

NOMENCLATURE

a	depth of impact damage or equivalent surface crack, m (in.)
A_{11}, A_{22}, A_{12}	Constants in Hertz equation, Pa (psi)
c	length of impact damage or equivalent surface crack, m (in.)
E_1, E_2	Young's moduli of isotropic impacter and target, Pa (psi)
E_{11}, E_{22}	Young's moduli of composite laminae parallel and normal to fiber direction, respectively, Pa (psi)
E_x, E_y	Young's moduli of FWC laminate, Pa (psi)
E_r, E_z	Young's moduli of transversely isotropic body, Pa (psi)
$f(\frac{a}{t}, \frac{a}{c}, \frac{c}{W}, \phi)$	functional in Eqs 11 and 12
F	contact force, N (lbf)
F_{max}	maximum contact force during impact, N (lbf)
G_{12}	Shear modulus of laminae, Pa (psi)
G_{xy}	Shear modulus of FWC laminate, Pa (psi)
G_{zr}	Shear modulus of transversely isotropic body, Pa (psi)

h	thickness, m (in.)
k_f	spring constant for flexure, N/m (lbf/in.)
k_1, k_2	factors in the Hertz law, Pa^{-1} $(psi)^{-1}$
K	stress intensity factor, Pa $mm^{1/2}$, (psi $in.^{1/2}$)
K_Q	fracture toughness, Pa $mm^{1/2}$, (psi $in.^{1/2}$)
KE_{eff}	effective kinetic energy, $\frac{1}{2} M v_1^2$, J (ft-lbf)
m_1, m_2	mass of impacter and target, kg (lbm)
M	effective mass, kg (lbm)
n_o	factor in the Hertz law, Pa (psi)
p	contact pressure, Pa (psi)
p_c	average contact pressure, Pa (psi)
Q	shape factor for an elliptical crack
r_c	contact radius, m (in.)
R_1	radius of impacter, m (in.)
S_x	hoop stress, Pa (ksi)
S_{xc}	hoop stress at failure, Pa (ksi)
t	time, sec
u	relative displacement between impacter and target, m (in.)
u_i	indentation of target given by Hertz's law, m (in.)
u_f	displacement of target due to flexure, m (in.)
v_1, v_2	velocity of impacter and target, m/sec (in./sec)
W	width of specimen in test section, m (in.)
z_o	depth from surface where damage initiates
ν_{xy}, ν_{yx}	Poisson's ratios of FWC laminate
ν_r, ν_{rz}	Poisson's ratios of transversely isotropic semi-infinite body or target
ν_1, ν_2	Poisson's ratio of isotropic impacter and target
ν_{12}	principal Poisson's ratio of laminae
ζ	ratio z/r_c
ζ_o	ratio z_o/r_c
τ_u	shear strength, Pa (psi)
τ_{max}	maximum principal shear stress, Pa (psi)
ϕ	parametric angle of ellipse

Subscripts:

1, 2	principal coordinates of the FWC layers (The 1-direction is the fiber direction.)
x, y	Cartesian coordinates (The x-direction is the axial direction of the cylinder or hoop direction of the FWC laminate.)

r, θ, z cylindrical coordinates (The z-direction is normal to the laminate.)

Original measurements were made in English units and converted to SI units.

MATERIAL

A 0.76-m- (30-in.) diameter, 2.13-m- (7-ft) long cylinder was made by Hercules Inc. to represent the region of a FWC away from the ends. The thickness of the cylinder was the same as that of a FWC, 36 mm (1.4 in.). The directions of the hoop and helical layers in the cylinder are shown in Fig. 1. Notice that the hoop and helical directions were rotated 90° to provide straight specimens for uniaxial loading in the hoop direction. For this reason, the hoop layers could not be wound using the wet process but had to be hand laid using prepreg tape. (Reference to hoop layers in this paper is reference to fibers in the hoop direction of the FWC but in the longitudinal direction of the cylinder.) However, the helical layers were wound using a wet process like that used to make a FWC. The graphite fiber and winding resin were also the same used to make the FWC's. The fiber was AS4W-12K graphite, and the winding resin was HBRF-55A epoxy (Hercules Inc.'s designations). The prepreg tape was actually a unidirectional broadgoods. The epoxy in the prepreg was Hercules Inc.'s MX-16. Tests were conducted on fibers from each lot of material used to make the cylinder. Properties of the helical fiber, broadgoods fiber, and resin are given in Table 1. Properties of the prepreg and winding resins are the same. The helical and broadgoods fibers were from different lots. The physical properties and lamina constants, which were measured by Hercules Inc., are given in Tables 2 and 3, respectively.

From outside to inside, the orientations of the layers were $\{(\pm 56.5)_2/0/[(\pm\underline{56.5})_2/0]_3/[(\pm 56.5)_2/0]_7/(\pm 56.5/0_2)_4/(\pm 56.5)_2/\text{cloth}\}$, where the 0° layers are the hoops and the ±56.5° layers are the helicals. (The layer angles are measured from the axis of the cylinder.) The underlined $\pm\underline{56.5^\circ}$ helical layers are about 1.6 times as thick as the other helical layers. The cloth layer at the inner surface has an equal number of fibers in the warp and weave directions. The layup is balanced (equal numbers of +56.5° and -56.5° layers) but not symmetrical about the midplane. More hoop layers are near the inner surface than the outer surface.

The elastic constants of the cylinder are given in Table 4. They were predicted with lamination theory using the lamina constants in Table 3. In general, bending and stretching couple in an unsymmetric laminate like that of the FWC. However, for the axisymmetric case of a cylinder containing pressure, bending and stretching do not couple. Thus, the elastic constants were calculated assuming that the laminate is symmetric. The x- and y-directions in the subscripts of the elastic constants correspond to the axial and hoop directions of the cylinder. See Fig. 1.

The value of fracture toughness K_Q for the cylinder was 0.949 GPa $mm^{1/2}$ (27.3 ksi $in.^{1/2}$) [3-5]. A general fracture toughness parameter and the failing

strain of the fibers was used to predict K_Q. The crack was assumed to be normal to the hoop direction.

TEST APPARATUS AND PROCEDURE

Impact Tests

The cylinder was cut into seven 30.5-cm- (12-in.) long rings. The rings were impacted by free-falling masses. See Fig. 1. Inert propellant was cast in several of the rings, but the others were left empty. The masses of an empty and a filled ring were 40 kg (89.1 lbm) and 288 kg (635 lbm), respectively. During impacts, the rings lay on a thin rubber sheet in a shallow aluminum cradle. The bottom of the empty ring was secured to the concrete floor with a cross-bar to prevent the ring from "leaping" off the floor when impacted. Each ring was impacted every 51 mm (2.0 in.) of circumference, giving 44 impact sites. The damaged regions did not overlap.

The free-falling impacter was a 51-mm- (2-in.) diameter steel rod with indenters of several shapes attached to one end. The indenters were a 12.7-mm- (0.5-in.) diameter hemisphere and a sharp corner. The tip of the corner indenter had a radius less than 0.25 mm (0.01 in.). The mass of the impacter was 5.0 kg (11.1 lbm), including the indenter. The impacter was instrumented to determine the maximum impact force. Drop heights were varied from 36 to 274 cm (14 to 108 in.) to give kinetic energies from 17 to 136 J (13 to 100 ft-lbf). After each impact, the ring was rotated to present a new site. Each ring had a total of 44 impact sites. Some sites on each ring were not impacted but reserved as undamaged specimens for determining mechanical properties. After the impacts were completed, each ring was cut into 44 tension specimens that were oriented as shown in Fig. 1. The center of each specimen coincided with an impact site. The cut edges were ground flat and parallel so that the width and length of the specimens were 51 mm (2.0 in.) and 31 cm (12 in.), respectively.

Simulated Impact Tests

No rings remained for impacts using other indenters. Thus, nine of the 51-mm (2.0-in.) by 30.5-cm (12-in.) tension specimens that were reserved for tests to determine mechanical properties were used instead for simulated impact tests with a rod shaped indenter. The impacts were not made by dropping weights because of a potential difference between the dynamic response of the ring and that of the small tension specimen. The rod indenter had a diameter of 6.3 mm (0.25 in.). The corner of the rod (intersection of the side and end) had a radius of 1.3 mm (0.05 in.) to simulate the end of a bolt. The impacts were simulated by mounting the rod indenter in the upper grip of a hydraulic testing machine and slowly pressing the rod against the face of the straight-sided tension specimens. Stroke was programmed to increase linearly with time. The maximum strokes were 3.4, 6.5, and 9.5 mm (0.135, 0.255, and 0.375 in.) for three specimens each. Load and stroke were recorded on an x-y recorder.

X-Ray Tests

The impacted face of each specimen (including those with simulated impacts) was soaked in a zinc iodide penetrant for 30 sec, and radiographs were made from the impacted side. The penetrant was contained by a circular dam on the surface of the specimen. The depth of impact damage in the radiographs was measured. After the specimens were X-rayed, circular arcs were ground into the specimens' edges to reduce the width in the test section to 38 mm (1.5 in.). See Fig. 2. Without the reduced width in the test section, the failure of specimens with small damage seemed to originate at the grips [2-4]. The width of the specimens was reduced in the test section to assure that failure originated at the impact damage and not at the edge of the grips where the stresses were elevated by the grip pressure [2-4].

Residual Strength Tests

The specimens were uniaxially loaded to failure in tension with a 445-kN-capacity (100 kips) hydraulic testing machine. Stroke was programmed to increase with time at the rate of 0.0076 mm/sec (0.0003 in./sec). Time to failure was several minutes at this rate. Hydraulically actuated grips that simulate fixed-end conditions were used. Otherwise, uniaxial loading would cause bending because the FWC laminate is not symmetrical.

ANALYSIS AND RESULTS

The experimental results are given in Tables 5-9 for the various indenters. The tables include kinetic energy of impacter $\frac{1}{2} m_1 v_1^2$, maximum impact force F_{max}, damage depth from radiograph, and tensile failure loads. Preliminary results revealed that differences between values of kinetic energy and potential energy of the impacter were less than the experimental accuracy. Thus, for convenience, values of kinetic energy were assumed to be equal to potential energy. For the rod indenter, the area under the load-displacement curve is reported for the kinetic energy. When the impacted specimens were loaded to failure in tension, those with very shallow damage (outermost helical layers or less) failed catastrophically in one stage [3-5]. However, those with deeper damage (one or more hoop layers) failed in two stages: first, the damaged layers failed and delaminated from the undamaged layers; and then, with additional load, the undamaged layers failed. The two stages of failure were referred to as first- and remaining-ligament failure. Loads are given in the tables for both failures when applicable.

Impact Force

The impact force increases with time to a maximum value and then decreases to zero, much as a haversine. For impacts to the thick composite rings, the time for the impact force to reach a maximum value was usually less than one

millisecond [2-4]. Assuming Hertzian contact and Newtonian mechanics, the maximum impact force F_{max} is given by

$$\frac{1}{2\ k_f} F_{max}^2 + \frac{2}{5} R_1^{-1/3}\ n_0^{-2/3}\ F_{max}^{5/3} - KE_{eff} = 0 \tag{1}$$

where R_1 is the radius of the impacter, n_0 is a Hertzian constant defined by Eq 20, and k_f is a spring constant for the ring defined by Eq 18. The effective kinetic energy of the impact KE_{eff} is defined by

$$KE_{eff} = \frac{1}{2} M v_1^2 \tag{2}$$

where M is the effective mass defined by Eq 16 and v_1 is the velocity of the impacter. The derivation of Eqs 1 and 2 are given in the Appendix. Values of $n_0 = 4.52$ GPa (656 ksi) for filled and empty rings, $k_f = 5.08$ MN/m (29.0 kips/in.) for empty rings, and $k_f = 6.34$ MN/m (36.2 kips/in.) for filled rings were determined by tests. Details are given in the Appendix.

The results from the formulation of the impact problem here and in [11] are significantly different. In [11] it was assumed that the velocities of the impacter and target are equal during contact. Conservation of momentum was used to obtain the velocity during contact. Using the same initial and final conditions as those in the Appendix, one arrives at an equation with a form similar to that of Eq 1 but with

$$KE_{eff} = \frac{1}{2} m_1 v_1^2/(1 + \frac{1}{4} m_2/m_1) \tag{3}$$

rather than Eq 2, which also can also be written

$$KE_{eff} = \frac{1}{2} m_1 v_1^2/(1 + 4\ m_1/m_2) \tag{4}$$

The mass ratio $4\ m_1/m_2$ in Eq 4 is inverted relative to that in Eq 3. Thus, the effect of target mass on impact force in [11] is opposite to that in the present formulation.

Values of impact force are plotted against effective kinetic energy in Fig. 3 for a 25.4-mm- (1.0-in.) diameter hemisphere [3,4]. Each symbol is an average of several tests. The impact forces for the empty and filled rings coalesce quite well when plotted against the effective kinetic energy. For all values of KE_{eff} less than that labeled nonvisible damage (NVD), the impacts did not cause visible damage on the surface. For values of KE_{eff} greater than this threshold, the impacts caused a visible crater. Near the threshold, the craters were very shallow but perceptible. The depth of the craters increased with increasing KE_{eff}. Values of impact force calculated with Eq 1 and $n_0 = 4.52$ GPa (656 ksi) are also plotted. Curves are shown for three values of ring

stiffness: k_f = 5.08 MN/m (29.0 kips/in.), 6.34 MN/m (36.2 kips/in.), and ∞. For $k_f = \infty$, the ring does not flex at all in a global sense. When damage is nonvisible, the predicted curve for $k_f = \infty$ agrees with the test results quite well. But when damage is great enough to be visible, the actual impact forces are somewhat less than the predicted values. Values of impact force predicted with quasi-static values of k_f are much too small. The quasi-static values of k_f greatly overestimate the deflection of the rings during impact. Thus, the natural vibration periods of the rings were probably the same order of magnitude as the duration of the impacts, which was only a few milliseconds [3,4].

Values of impact force are plotted against effective kinetic energy KE_{eff} in Fig. 4 for the 12.7-mm- (0.5-in.) diameter hemisphere, the corner, and the rod indenters. For the simulated impacts with the rod indenter, the area under the load-displacement curve was used for KE_{eff}. Results for the 25.4-mm- (1.0-in.) diameter hemisphere in Fig. 3 are also plotted for comparison. Each symbol is an average of several tests. For a given KE_{eff}, impact force decreases with decreasing radius or increasing sharpness of the impacter. Filled and open symbols represent visible and nonvisible damage, respectively. The damage on the surface consisted of craters shaped like the indenters. The corner and rod indenters made craters for all impacts. The depth of the craters for all indenters increased with increasing KE_{eff}. For the hemispherical indenters, the thresholds for NVD are labeled as in Fig. 3. In the neighborhood of the thresholds, the craters were shallow. For a given value of KE_{eff}, the depth of the craters was greater for the smaller hemisphere. Except for the rod indenter, values of impact force calculated with Eq 1 are also plotted. The calculations were made using k_f = 219 MN/m (1250 kips/in.) and n_0 = 4.52 GPa (656 ksi). This value of k_f, which was chosen so that Eq 1 would best agree with the data for hemispherical impacters with nonvisible damage, is much larger than the values determined by quasi-static tests. As a result, the term containing k_f in Eq 1 contributes very little to KE_{eff} as evident by comparing this curve with that in Fig. 3 for $k_f = \infty$. In Fig. 4, the difference between the curves for the two different hemispheres is not large for nonvisible damage, as predicted by Eq 1. On the other hand, impact forces for both hemispheres are less than predicted when the damage is visible. The dashed lines, which were fit to the data with visible damage, were assumed to have the same slope for both hemispheres. The test data for the 25.4-mm- (1.0-in.) diameter hemisphere do not have a sufficient range of KE_{eff} to confirm this assumption. Calculations were made for the corner by representing it as a hemisphere with a diameter of 0.61 mm (0.024 in.). This diameter was chosen to give the best agreement between predictions and tests. The actual radius of the tip was about half this value, approximately 0.25 mm (0.01 in.). The test data are modeled quite well by Eq 1 even though the indenter made a deep crater on the surface and the corner was represented as a hemisphere. Even though the agreement is probably fortuitous, the corner was represented as a small hemisphere in subsequent calculations of damage size to determine the limits of this representation. The slopes of the lines that represent test data with

visible damage in Fig. 4 vary with indenter shape. Thus, impact force for one indenter shape is not always less or greater than that for another shape for all values of KE_{eff}.

Damage

For Hertzian contact [12], the contact pressure between a hemispherical impacter of radius R_1 and a semi-infinite, transversely isotropic body is given by

$$p = \frac{3}{2} p_c \left(1 - \frac{r^2}{r_c^2}\right)^{1/2} \tag{5}$$

where r is the radius (polar coordinate) measured from the center of the contact site, r_c is the contact radius given by

$$r_c = \left(\frac{F_{max} R_1}{n_0}\right)^{1/3} \tag{6}$$

and p_c is the average pressure given by

$$p_c = \frac{F_{max}}{\pi r_c^2} \tag{7}$$

Using the theory of elasticity, Love [13] obtained a closed form solution for the internal stresses in a semi-infinite, isotropic body produced by the "hemispherical" pressure given by Eq 5. The problem is axisymmetric. Even though the composite is made of orthotropic layers, the results for the isotropic half space should at least be applicable in a qualitative sense. Contours of maximum shear stress = 228 MPa (33.0 ksi) and maximum compression stress = 587 MPa (85.1 ksi) were calculated using the equations in [13] with $\nu = 0.3$ and plotted in Fig. 5 for various values of average contact pressure. The maximum compression stress is in the plane of the composite layers, but the shear stress is generally not. Along the centerline, for example, the maximum shear stress lies in a plane that is inclined at 45^0 to the surface. The depth from the surface and distance from the center of contact are normalized by the contact radius r_c. For a given contact pressure, each contour represents the outermost extent of damage according to the maximum shear or maximum compression stress criterion. Since the stresses from Love's solution do not account for damage, they are valid only for predicting the onset of damage. Thus, the contours only give the approximate size of the damage region. Notice that damage initiates on the axis of symmetry. For the maximum shear stress criterion, damage initiates below the surface at a normalized depth of 0.482 for $p_c = 490$ MPa (71.1 ksi); whereas, for the maximum compression stress criterion,

damage initiates at the surface for p_c = 487 MPa (70.6 ksi). Therefore, damage initiates at a critical contact pressure, independent of impacter radius.

The maximum depth of the damage contours for maximum shear stress in Fig. 5 is given by

$$(\tfrac{1}{2} - \nu_t)(1 + \zeta^2)^{-1} + (1 + \nu_t)[\zeta \operatorname{Tan}^{-1}(\tfrac{1}{\zeta}) - \zeta^2(1 + \zeta^2)^{-1}] - \frac{4\tau_u}{3p_c} = 0 \qquad (8)$$

where $\zeta = a/r_c$. The depth $\zeta_0 = z_0/r_c$, which corresponds to the location of τ_{max} and damage initiation, is given by[1]

$$3\zeta_0 - (1 + \nu_t)(1 + \zeta_0^2)[(1 + \zeta_0^2)\operatorname{Tan}^{-1}(\tfrac{1}{\zeta_0}) - \zeta_0] = 0 \qquad (9)$$

The size of the damage in Fig. 5 and Eqs 8 and 9 are normalized by the contact radius. The contact radius r_c can be written in terms of the average contact pressure p_c instead of the maximum impact force F_{max}. Using Eq 7 to eliminate F_{max} in Eq 6 results in

$$r_c = \frac{\pi\, p_c\, R_1}{n_0} \qquad (10)$$

Thus, r_c increases in proportion to p_c and impacter radius R_1. Hence, the absolute size of the damage contours in Fig. 5 increases in proportion to p_c and R_1. Thus, for a given pressure above the critical level, the depth and width of damage increase in proportion to impacter radius.

Since damage is predicted to initiate on or near the surface for a constant value of average contact pressure, damage should also become visible on the surface for a constant value of average contact pressure, at least for hemispherical indenters. Accordingly, contact pressures are plotted against impact force in Fig. 6 for the various indenters. The contact pressures were calculated using Eqs 6 and 7 and the measured values of impact force in Fig. 4. The value of n_0 was assumed to be 4.52 GPa (656 ksi). The corner indenter was again represented as a 0.61-mm- (0.024-in.) diameter hemisphere. For the 6.5-mm- (0.25-in.) diameter rod indenter, the contact area was assumed to be equal to the full area of the rod's cross section -- not the reduced area at the end.

---

1 The equation in [5,10] that corresponds to Eq 8 in this report contains an error. The author also discovered a discrepancy between Eqs 8 and 9 in this report and results reported in [14]. It is believed that the sign of the second term in Eq 20a of [14] should be reversed.

Filled and open symbols represent visible and nonvisible damage, respectively. The lines were fit to the data. Indeed, the critical pressure to cause visible damage for the 25.4-mm- (1.0-in.) diameter hemisphere was only about 7 percent greater than that for the 12.7-mm- (0.5-in.) diameter hemisphere. The dashed horizontal line in Fig. 6 represents a critical pressure of 705 MPa (102 ksi). Contact pressures for all tests with the corner and rod indenters exceeded 705 MPa (102 ksi) and damage was visible like that for the hemispheres. The slope of the curve for the rod indenter was greater than that for the other indenters because contact area was a constant, whereas contact area increases with impact force to the two-thirds power for a hemisphere.

Fiber Damage

To verify radiographic and ultrasonic measurements of impact damage in the rings, specimens from an actual FWC were impacted and pyrolyzed. The pyrolysis removed most of the epoxy, facilitating the separating of layers or deplying of the composite. The results were reported in [10]. The impacts were simulated by quasi-statically pressing a hemispherical indenter against the specimen's face, much like the simulated impacts with the rod indenter in the present investigation. Photographs of the outermost 9 deplied layers from one specimen are shown in Fig. 7. The layers contain broken fibers, the locus of which resembles cracks. The layer samples were 38 by 38 mm (1.5 by 1.5 in.). The "cracks" were visible in the 15 outermost layers, of which the outermost 9 are shown in Fig. 7. These cracks were mostly parallel to the direction of fibers in the neighboring layers. By coincidence, the cracks appear to be nearly normal to the fibers in the layer in which they reside. When the fibers in the neighboring layers were not parallel to each other, the direction of the cracks wandered between the direction of the fibers in the each neighboring layer. For this sample, a 50.8-mm- (2.00-in.) diameter hemispherical indenter was used to produce a contact force of 267 kN (60.0 kips) and a contact pressure of 648 MPa (94.0 ksi). The simulated impact caused a visible crater on the surface.

Several specimens in [10] were not deplied but were sectioned through the thickness and examined using a scanning electron microscope. Photomicrographs of two sections from the same depth are shown in Fig. 8. This impact was also simulated with the 50.8-mm- (2.00-in.) diameter hemisphere, producing a contact force of 200 kN (45.0 kips) and a contact pressure of 589 MPa (85.4 ksi). A crater was visible on the surface. The section on the left in Fig. 8 is directly below the contact area, and the section on the right is outside the contact area. The sections are normal to the plane of the hoop layers and parallel to the direction of the hoop fibers. An edge of the outermost hoop layer can be seen at the center of both sections. The section on the left reveals several matrix cracks in the helical layers on both sides of the hoop layer. The cracks are located in the plane of maximum shear stress. The matrix shear cracks continue across the hoop layer and thus break the fibers. This combination of matrix shear cracks and broken fibers was typical in the other sections as well. Fiber kinking in the hoop layer, which is associated with in-plane compression failure, can be observed in the section on the right. A rather large void lies above the kinked fibers, and what appears to be a delamination lies below. This delamination is probably a lack of bond caused by the manufacturing process rather than by the simulated impact. This type of delamination was not unusual in the many FWC's that were made. Thus, the fiber

kinking is probably a result of the inplane compression stress due to the simulated impact combined with the lack of matrix support to the fibers.

The maximum depths of fiber breaks for the deplied specimens from [10] are plotted in Fig. 9. Each symbol is an average of several tests. The damage depth was normalized by the contact radius. The filled symbols indicate visible damage on the surface, and the open symbols indicate nonvisible damage. The maximum depths of the contours in Fig. 5 are also plotted in Fig. 9 for comparison. The compression allowable in Fig. 5 is based on the failing strain and Young's modulus of the composite. The shear allowable was chosen to give an upper bound to the damage depths in Fig. 9. Compression tests [10] gave an ultimate shear strength of 310 MPa (45.0 ksi), which would have moved the curve for maximum shear stress to the right by 0.178 GPa (25.8 ksi) in Fig. 9 and would have given a lower bound to the test data. The envelope of predicted damage depth is represented by the solid line. The damage far below the surface corresponds to the maximum shear stress criteria, and the damage near the surface corresponds to the maximum compression stress criteria. The maximum stress criteria represent the data quite well considering that the composite is neither homogeneous nor isotropic. Widths of the contours in Fig. 5 are approximately 1.6 times the depth [10]. The widths (crack lengths) from the tests were 2 to 3 times the depths. Hence, the maximum stress criteria tended to underpredict the width of damage, probably an effect of the transversely isotropic nature of the composite.

The maximum depths of impact damage from radiographs of the impacted specimens are plotted in Fig. 10. Recall that impacts with the rod indenter were simulated. Each symbol is an average of several tests. The data for the 25.4-mm- (1.0-in.) diameter impacter are from [3,4]. The damage depth was normalized by the contact radius calculated with Eq 6. The filled symbols indicate visible damage on the surface, and the open symbols indicate nonvisible damage. Logarithmic scales are used because of the wide range of values for the various impacters. The maximum depths of the contours in Fig. 5 are also plotted in Fig. 10 for comparison. As with the deply data for simulated impacts, the radiographic data for the hemispheres and corner follow the maximum stress criteria quite well. The agreement for the corner indenter is better than anticipated considering that it was represented as a small hemisphere. The rod indenter produces uniform displacements on the surface, which result in infinite stresses at the edge of the rod compared to finite stresses at the edge of the contact region of the hemisphere. (See [14] for an excellent review of the contact problem.) Thus, the rod indenter acts like a punch and slices through the composite. Consequently, the depth of damage is greater than that predicted for the hemisphere.

Values of average contact pressure are plotted against stroke (displacement of the actuator) in Fig. 11 for three of the simulated impact tests with the rod indenter. Again, the full area of the rod's cross section was used to calculate pressure. The stroke is approximately equal to indentation. These curves are typical for the rod indenter. Notice that each curve is smooth until reaching pressures between 600 and 650 MPa (87 and 94.3 ksi) where a jump in displacement occurs. These jumps probably correspond to damage initiation. These pressures are only slightly more than the lowest pressure that resulted in damage for the hemispheres in Fig. 10. Thus, the critical level of contact pressure to initiate damage is essentially the same for the rod and hemisphere indenters. Since the pressures to initiate damage are about the same for the two indenter

shapes, it is expected that the pressures to cause visible damage are also about the same. Notice that the displacement in Fig. 11 increases dramatically once damage develops because the rod indenter penetrates like a punch.

In Fig. 12, values of actuator stroke and damage depth for the rod indenter are plotted against average contact pressure. Except for the largest value of stroke, the damage extends ahead of the rod indenter, much as it does for the hemispheres. Some specimens were delaminated completely at the bottom of the damage as a result of the simulated impact. On the other hand, large delaminations were not found in specimens impacted with the other indenters. Perhaps the large amount of damaged material pushed ahead of the rod caused the delamination.

Impact damage from the 25.4-mm- (1.0-in.) diameter hemisphere was difficult to see in radiographs [3-9]. A comparison between damage depth determined by deply [10] and radiographs for the 12.7- and 25.4-mm- (0.5- and 1.0-in.) diameter hemispheres is made in Fig. 13 and 14. The radiographic data for the 25.4-mm- (1.0-in.) diameter hemisphere is from [3,4]. The impacts were simulated for the deply data but not for the radiographic data. The maximum depth is normalized by contact radius and plotted against average contact pressure. The contact radius was calculated with Eq 6. The predictions made with the maximum stress criteria are also plotted for a reference. The deply and radiographic results are in good agreement for the 25.4-mm- (1.0-in.) diameter hemisphere. However, for the 12.7-mm- (0.5-in.) diameter hemisphere, the depths from radiographs are much smaller than those from the deply tests and do not coalesce with depths for the 25.4-mm- (1.0-in.) diameter hemisphere as the maximum stress criteria predict. On the other hand, the thresholds for nonvisible damage for radiographs and deply tests are in agreement for the two hemispheres. The difference between results for the radiographs and deply tests is not likely due to the difference between impacts and simulated impacts but rather due to the x-ray opaque dye not penetrating to the innermost damage [3,4,6] and to the small size of the damage. In impact tests with the 12.7-mm- (0.5-in.) diameter hemisphere where the contact pressures were high, local heating was sufficient to pyrolyze the epoxy matrix. The higher temperatures may have made the damage less penetrable. Pressures were generally lower for the 25.4-mm- (0.5-in.) diameter hemisphere and no pyrolysis was noticed. Regarding damage size, the volume of damaged material and dye for the 25.4-mm- (1.0-in.) diameter hemisphere is 8 times that for the 12.7-mm- (0.5-in.) diameter hemisphere. (Recall that the depth and radius of the damaged region increases in proportion to hemisphere radius for a given contact pressure.) Hence, more x-rays are attenuated for damage from the larger hemisphere than from the smaller one, and the contrast between damaged and undamaged material is greater. Therefore, damage from the 12.7-mm- (0.5-in.) diameter hemisphere is more difficult to see in a radiograph than that from the 25.4-mm- (1.0-in.) diameter hemisphere.

The critical contact pressure to cause visible damage did vary somewhat with hemisphere diameter. Average contact pressures from Figs. 9 and 10 are plotted against hemisphere diameter in Fig. 15. Different symbols are used to indicate visible and nonvisible damage. The average contact pressure to cause visible damage increased somewhat with decreasing hemisphere diameter, particularly for the deply tests where the variation of diameter is greatest. Because the contact radius increases in proportion to hemisphere radius for a given contact pressure (Eq 10), the surface area of damaged material increases

in proportion to the square of the hemisphere diameter. Thus, the surface damage caused by a large hemisphere is more visible than that caused by a small hemisphere. Hence, there is no contradiction between damage initiation being independent of hemisphere radius and damage visibility increasing with increasing hemisphere radius.

The impacter diameter is plotted against effective kinetic energy for constant values of contact pressure in Fig. 16. The curves were calculated using Eq.s 1, 6, and 7 for the pressures that correspond to thresholds for damage initiation 490 MPa (71.1 ksi) and damage visibility 705 MPa (102 ksi). Values of n_0 = 4.52 GPa (656 ksi) and k_f = 219 MN/m (1250 kips/in.) were used. Equation 1 should be reasonably accurate for $p_c \leq 705$ MPa (102 ksi), since damage is small. The curves divide the graph into regions of no damage, nonvisible damage, and visible damage. Along these curves, the effective kinetic energy increases approximately with impacter diameter to the third power. Thus, for large impacter diameters, very large energies are necessary to initiate damage. Also, the region of nonvisible damage is quite large. For a given value of effective kinetic energy, the ratio of impacter diameters for the upper and lower curves is approximately 1.8; and, for a given value of impacter diameter, the ratio of effective kinetic energies for the upper and lower curves is approximately 0.16. Test data for the two hemispheres and the corner and rod indenters are plotted for comparison. The agreement between the tests and predictions verifies the use of simple mechanics and Hertzian contact to predict the effect of indenter size and shape.

Residual Strength

As noted previously, when the impacted specimens were loaded to failure in tension, those with very shallow damage (outermost helical layers or less) failed catastrophically in one stage [3-5]. But, those with deeper damage (one or more hoop layers) failed in two stages: first, the damaged layers failed and delaminated from the undamaged layers; and then, with additional load, the undamaged layers failed. The two stages of failure were referred to as first- and remaining-ligament failure. Only the first-ligament strengths will be considered here because they are the lowest. The first-ligament strengths were predicted by representing the impact damage as a semi-elliptical surface crack in a plane normal to the hoop direction. The depth of the equivalent crack was calculated with Eq 8. The length of the equivalent crack was assumed to be equal to the depth. The singular stresses along the crack front are proportional to the stress intensity factor K. For a semi-elliptical surface crack in an isotropic plate with membrane loading, K is given by

$$K = S_x \left(\frac{\pi a}{Q}\right)^{1/2} f\left(\frac{a}{h}, \frac{a}{c}, \frac{c}{W}, \phi\right) \tag{11}$$

where Q is the shape function, S_x is the hoop stress, a is the equivalent crack depth, c is the equivalent crack length, and $f\left(\frac{a}{h}, \frac{a}{c}, \frac{c}{W}, \phi\right)$ corrects for the finite thickness h and width W of the specimen. The thickness h was 36 mm (1.4 in.), and the width W was 38 mm (1.5 in.). The stress intensity factor K, which varies along the crack front with the parametric

angle ϕ, is greatest at the point where the crack intersects the free surface ($\phi = 0^0$) or at the maximum depth ($\phi = 90^0$), depending on the ratio a/c. The functionals Q and $f(\frac{a}{h}, \frac{a}{c}, \frac{c}{W}, \phi)$ are given in [3-5,15].

At failure, $K = K_Q$ and $S_x = S_{xc}$ where K_Q is the fracture toughness and S_{xc} is the strength. Solving Eq 11 for S_x and making the substitutions $K = K_Q$ and $S_x = S_{xc}$ results in

$$S_{xc} = K_Q \left(\frac{\pi a}{Q}\right)^{-1/2} f\left(\frac{a}{h}, \frac{a}{c}, \frac{c}{W}, \phi\right)^{-1} \tag{12}$$

Values of strength associated with first-ligament failure were divided by the undamaged strength of 345 MPa (50.1 ksi) and plotted against impact force in Fig. 17. The test values of strength, which are plotted as symbols, were calculated by dividing the failure loads by the thickness h = 36 mm (1.4 in.) and width W = 38 mm (1.5 in.) of the test section. See Fig. 2. Each symbol is an average of several tests. A different symbol was used for each indenter with open symbols representing nonvisible damage and filled symbols representing visible damage. The test data for the 25.4-mm- (1.0-in.) diameter hemisphere was taken from [3,4]. Calculations with Eq 12 were plotted as lines, which are dashed to indicate nonvisible damage, $p_c < 705$ MPa (102 ksi), and solid to indicate visible damage, $p_c \geq 705$ MPa (102 ksi). The strengths for the corner indenter were predicted by representing it as a 0.61-mm- (0.024-in.) diameter hemisphere. No strengths were predicted for the rod indenter. The predictions and tests are in reasonably good agreement, even for the corner. The residual strengths for the rod indenter are lowest because of the penetration and hence deep damage. Notice that the strength was reduced as much as 9 and 30 percent by the 12.7-mm- (0.5-in.) and 25.4-mm- (1.0-in.) diameter hemispheres, respectively, without causing visible damage. The locus of predictions for $p_c = 705$ MPa (102 ksi), which represents the lowest strengths with nonvisible damage, is also plotted in Fig. 17 as a dash-dot line. About one third of the open symbols lie below this curve due to the scatter in strengths. Thus, the curve for $p_c = 705$ MPa (102 ksi) is in good agreement with the test data on the average.

The factor of safety for impact damage is given by the ratio of undamaged strength to damaged strength. Reciprocals of the strength ratios for the test data in Fig. 17 are plotted against KE_{eff} in Fig. 18. The curve for $p_c = 705$ MPa (102 ksi) in Fig. 17 is plotted as a solid line. The values of KE_{eff} were calculated with Eq.s 1 and 2 using $n_o = 4.52$ GPa (656 ksi) and $k_f = 219$ MN/m (1250 kips/in.). For the simulated impacts with the rod indenter, KE_{eff} was assumed to be equal to the area under load-stroke curves. The predicted curve for $p_c = 705$ MPa (102 ksi) corresponds to a factor of safety for nonvisible damage. For this factor of safety, all nonvisible damage would be acceptable, but all visible damage would be unacceptable and have to be detected and repaired. As in Fig. 17, the predicted curve and open symbols are in agreement on the average due to the scatter in strengths. A design curve should lie above

all the open symbols. Accordingly, the dashed curve was drawn through the locus of highest open symbols. The predicted curve was used as a guide. The dashed curve represents a minimum factor of safety based on the test data.

In Fig. 18, the predicted factor of safety for nonvisible damage increases with increasing KE_{eff}. Thus, in design, one would choose the factor of safety corresponding to the condition with the largest KE_{eff}. The corresponding impacter diameters for no damage, nonvisible damage, and visible damage can be determined from Fig. 16. If the smallest possible impacter diameter were in the no-damage region or the largest possible impacter diameter were in the visible damage region, nonvisible damage could not occur and the factor of safety would be unity. However, most environments are not that restrictive, and the factor of safety for nonvisible damage would usually be greater than unity. The factor of safety for the membrane of the FWC was 1.4. Thus, nonvisible damage was acceptable for $KE_{eff} \leq 123$ J (91 ft-lbf). See Fig. 18.

Although the investigation here and in [2-4] was conducted with impacts from small objects like tools and equipment in mind, designs should also account for the structure moving. The results here can be applied if the velocity of the structure is set equal to v_1 in Eq 2, and the mass of the stationary object is assumed to be concentrated at it's centroid. (The velocity v_1 in Eq 2 can be replaced by the relative velocity between the impacter and target.) The longest FWC's had a mass of about 4,500 kg (10,000 lbm) empty and about 140,000 kg (300,000 lbm) when filled with propellant. Thus, the potential energy or kinetic energy of one of these FWC's is very large when they are being moved, 44,000 J (33,000 ft-lbf) for an empty FWC lifted 1 m (39 in.). The energy for a filled FWC would be 30 times that for an empty FWC. For kinetic energy exceeding 2,000 J (1,500 ft-lbf), the predicted minimum factor of safety in Fig. 18 would exceed two. Thus, the factor of safety for nonvisible damage can be greater for handling accidents than for dropped tools and equipment.

The analytical methods used here to predict impact damage and residual strength could be used to perform sensitivity studies and to evaluate material improvements analytically, for example, variations in n_o, τ_u, and K_Q. Design curves, like the dashed curve in Fig. 18, can also be established experimentally for other composites and other thicknesses. Kinetic energies need only be large enough to exceed the threshold for visible damage. The range of test parameters could be established analytically with the methods used here.

CONCLUSIONS

The relevance of impacter shape to nonvisible damage and residual tensile strength was determined for thick graphite/epoxy rocket motor cases of the Space Shuttle. The impacter shapes included hemispheres with 12.7- and 25.4-mm (0.5- and 1.0-in.) diameters, a 6.3-mm- (0.25-in.) diameter bolt-like rod, and a sharp corner. The cases were represented by rings (short cylinders) that were 30.5-cm (12-in.) long and 36-mm (1.4-in.) thick. The rings were cut from a 2.13-m- (7-foot) long cylinder that was wet-wound on a 76.2-cm- (30-in.) diameter mandrel using AS4 graphite fibers and an epoxy resin. A 5 kg (11.1 lbm) instrumented

impacter was dropped from various heights onto the rings, which were either empty or filled with inert propellant. After the rings were impacted numerous times around the circumference, they were cut into 51-mm- (2-in.) wide specimens that were loaded uniaxially in tension to failure. The damage was always local to the impact site and never extended into neighboring impact sites.

For the hemispherical impacters, damage initiated and became visible on the surface when the peak contact pressure during the impact event exceeded a critical level. The damage on the surface consisted of a crater shaped like the indenter and the damage below the surface consisted of brokens fibers that appeared to be caused by shear failure of the matrix. The damage initiated below the surface before it became visible on the surface. The pressure level to cause visible damage was about 1.4 times that to initiate damage. The extent of nonvisible damage and the resulting reduction in strength increased with increasing impacter diameter. For the 12.7-mm- (0.5-in.) and 25.4-mm- (1.0-in.) diameter hemispheres, the reductions in strength were 10 and 30 percent, respectively. The corner impacter acted like a hemisphere with a very small diameter and caused visible damage for even the smallest values of kinetic energy. The rod impacter acted like a punch and sliced through the composite. Nevertheless, the critical level of pressure to initiate damage was about equal for the rod and hemispherical impacters.

The depth and width of impact damage was predicted assuming Hertzian contact and maximum stress criteria. Internal stresses were calculated using theory of elasticity. The impact damage was represented as a surface crack with the same depth and length, and residual strengths were predicted using surface crack analysis. The corner was represented as a hemisphere with diameter of 6.3 mm (0.25 in.). Strengths were not predicted for the rod impacter. Factors of safety predicted for nonvisible damage increased with increasing kinetic energy of impact. The size of damage and residual strengths for the hemispheres and corner were predicted quite well. Ground handling accidents can involve much more energy than tool drops, requiring a much larger factor of safety for nonvisible damage.

APPENDIX - DERIVATION OF EQUATION FOR MAXIMUM IMPACT FORCE

The mass and velocity of the impacter and ring are denoted by m_1, v_1 and m_2, v_2, respectively. Because the mass of the rings is distributed, only a portion of the mass will act at the contact point. For example, when a simply supported beam is impacted transversely at the center [11], the "effective" mass is approximately 1/2. Based on rebound velocities for impacters of various masses, the effective masses of the empty and filled rings were found to be approximately 1/4 the total mass [3,4].

The following formulation of the impact problem is taken from [12] with the mass of the ring m_2 replaced by the effective mass $m_2/4$. The mass of the impacter is assumed to be fully effective, that is, concentrated at the end. During contact, Newton's law gives

$$m_1 \frac{dv_1}{dt} = -F, \quad \frac{1}{4} m_2 \frac{dv_2}{dt} = -F \tag{13}$$

Denoting the relative displacement between the impacter and ring by u, the relative velocity can be written,

$$\frac{du}{dt} = v_1 + v_2 \tag{14}$$

Differentiating Eq 14 with respect to time and substituting Eqs 13 into the result,

$$\frac{d^2u}{dt^2} = -\frac{F}{M} \tag{15}$$

where

$$M = \frac{1}{\frac{1}{m_1} + \frac{4}{m_2}} \tag{16}$$

If the duration of the impact is long compared to natural periods of vibration, the relative displacement u in Eqs 14 and 15 can be written

$$u = u_f + u_i \tag{17}$$

where u_f is the global deflection of the ring due to flexure and u_i is the local indentation for Hertzian contact. The steel impacter is assumed to be rigid compared to the composite ring. The flexural component is represented by a linear spring,

$$u_f = \frac{F}{k_f} \tag{18}$$

where k_f is a spring constant.

For a spherical, isotropic body in contact with a semi-infinite body that is homogeneous and transversely isotropic, the local indentation from [12] is

$$u_i = R_1^{-1/3} \left(\frac{F}{n_0}\right)^{2/3} \tag{19}$$

where R_1 is the radius of the sphere. The term n_0 is defined as

$$n_0 = \frac{4}{3\pi (k_1 + k_2)} \tag{20}$$

where

$$k_1 = \frac{1 - \nu_1^2}{\pi E_1}$$

$$k_2 = \frac{A_{22}^{1/2}\{[(A_{11}A_{22})^{1/2} + G_{zr}]^2 - (A_{12} + G_{zr})^2\}^{1/2}}{2\pi G_{zr}^{1/2}(A_{11}A_{22} - A_{12}^2)}$$

$$A_{11} = \frac{E_z}{1 - \frac{2\nu_{rz}^2 E_z}{(1 - \nu_r) E_r}}$$

$$A_{22} = \frac{(\frac{E_r}{E_z} - \nu_{rz}^2) A_{11}}{1 - \nu_r^2}$$

$$A_{12} = \frac{\nu_{rz} A_{11}}{1 - \nu_r}$$

and ν_1 and E_1 are the elastic constants of the isotropic sphere and ν_r, ν_{rz}, E_r, E_z, and G_{zr} are the elastic constants of the transversly isotropic semi-infinite body. Equation 19 is accurate only when $u_i < R_1$.

Substituting Eqs 18 and 19 into 17 and differentiating with respect to time, the relative velocity is

$$\frac{du}{dt} = \frac{1}{k_f}\frac{dF}{dt} + \frac{2}{3} R_1^{-1/3} n_o^{-2/3} F^{-1/3} \frac{dF}{dt} \tag{21}$$

Multiplying Eq 15 by Eq 21 and using the identity $d(x^m)/dt = m x^{m-1} dx/dt$,

$$\frac{1}{2M}\frac{d}{dt}\left[\frac{(du)^2}{dt}\right] = -\frac{2}{5} n_o^{-2/3} R_1^{-1/3} \frac{d(F^{5/3})}{t} - \frac{1}{2k_f}\frac{d(F^2)}{d} \tag{22}$$

Integrating Eq 22 with initial conditions $du/dt = v_1$ and $F = 0$ and final conditions $du/dt = 0$ and $F = F_{max}$ yields

$$\frac{1}{2 k_f} F_{max}^2 + \frac{2}{5} R_1^{-1/3} n_o^{-2/3} F_{max}^{5/3} - KE_{eff} = 0$$

where

$$KE_{eff} = \frac{1}{2} M v_1^2$$

Calculations with Eq 20 give $n_0 = 4.69$ GPa (680 ksi) for the approximately transversely isotropic ring and steel impacter [10]. Values of n_0 were also determined experimentally by directly measuring contact radii and displacements. From the measurements of contact radii, the average value of n_0 was 3.98 GPa (577 ksi) [3-5]; and, from the displacement measurements, the average value of n_0 was 4.52 GPa (656 ksi) [10]. These values of n_0 agree quite well. The value $n_0 = 4.52$ GPa (656 ksi) was used in all subsequent calculations.

Values of the spring constant k_f were 5.08 MN/m (29.0 kips/in.) and 6.34 MN/m (36.2 kips/in.) for an empty ring and a filled ring, respectively [4]. They were determined from quasi-static load-displacement curves. The value of k_f for the filled ring is only 25 percent greater than that for the empty ring. Thus, the inert propellant, which has a Young's modulus of 1.2 to 34 MPa (0.18 to 5.0 ksi) depending on loading rate, did not contribute substantially to the static compliance of the ring.

REFERENCES

[1] Loyd, B. A.; and Knight, G. K.: Impact Damage Sensitivity of Filament-Wound Composite Pressure Vessels. 1986 JANNAF Propulsion Meeting, CPIA Publication 455 Vol. 1, August 1986, pp. 7-15.

[2] Poe, C. C., Jr.; Illg, W.; and Garber, D. P.: A Program to Determine the Effect of Low-velocity Impacts on the Strength of the Filament-wound Rocket Motor Case for the Space Shuttle. NASA TM-87588, September 1985.

[3] Poe, C. C., Jr.; Illg, W.; and Garber, D. P.: Tension Strength of a Thick Graphite/epoxy Laminate after Impact by a 1/2-In.-Radius Impacter. NASA TM-87771, July 1986.

[4] Poe, C. C., Jr.; and Illg, W.: "Strength of a Thick Graphite/Epoxy Rocket Motor Case After Impact by a Blunt Object," Test Methods for Design Allowables for Fibrous Composites, ASTM STP 1003, C. C. Chamis, Ed., American Society for Testing and Materials, Philadelphia, 1989. pp. 150-179. (Also in NASA TM-89099, February 1987 and in 1987 JANNAF Composite Motor Case Subcommittee Meeting, CPIA Publication 460, Feb. 1987, pp. 179-202.)

[5] Poe, C. C., Jr.: Surface Crack Analysis Applied to Impact Damage in a Thick Graphite/Epoxy Composite. Surface Crack Growth: Models, Experiments and Structures, ASTM STP 1060, W. G. Reuter, J. Underwood, and J. C. Newman, Jr., Eds., American Society for Testing and Materials, Philadelphia, 1990. (Also in NASA TM-100600, April 1988.)

[6] Poe, C. C., Jr.; Illg, W.; and Garber, D. P.: Hidden Impact Damage in Thick Composites. Proceedings of the Review of Progress in Quantitative Nondestructive Evaluation, Vol. 5B, pp. 1215-1225, 1986.

[7] Madaras, E. I.; Poe, C. C., Jr.; Illg, W.; and Heyman, J. S.: Estimating Residual Strength in Filament Wound Casings from Non-Destructive Evaluation

of Impact Damage. Proceedings of the Review of Progress in Quantitative Nondestructive Evaluation, Vol. 6B, pp. 1221-1230, 1986.

[8] Madaras, E. I.; Poe, C. C., Jr.; and Heyman, J. S.: Combining Fracture Mechanics and Ultrasonics NDE to Predict the Strength Remaining in Thick Composites Subjected to Low-Level Impact. 1986 Ultrasonics Symposium Proceedings, Ed. B. R. McAvoy, New York, Institute of Electrical and Electronic Engineers. Vol. 86CH2375-4, No. 2, pp. 1051-1059.

[9] Madaras, E. I.; Poe, C. C., Jr.; and Heyman, J. S.: A Nondestructive Technique for Predicting the Strength Remaining in Filament Wound Composites Subjected to Low-Level Impact. 1987 JANNAF Composite Motor Case Subcommittee Meeting, CPIA Publication 460, Feb. 1987, pp. 249-258.

[10] Poe, C. C., Jr.: Simulated Impact Damage in a Thick Graphite/Epoxy Laminate Using Spherical Indenters. American Society for Composite Materials. November 1988. (Also in NASA TM-100539, January 1988.)

[11] Timoshenko, Stephen P.: History of Strength of Materials, with a Brief Account of the History of Theory of Elasticity and Theory of Structure, Dover Publications, Inc., 1982, pp. 178-180.

[12] Greszczuk, Longin B.: Damage in Composite Materials due to Low Velocity Impact. Impact Dynamics, John Wiley & Sons, Inc., 1982, pp. 55-94.

[13] Love, A. E. H.: The Stress Produced in a Semi-infinite Solid by Pressure on Part of the Boundary. Phil. Trans. Roy. Soc. Lond. Series A, Vol. 228, 1929, pp. 377-420.

[14] Johnson, K. L.: One Hundred Years of Hertz Contact. Proceedings of The Institution of Mechanical Engineers, Vol. 196 No. 39, 1982, p. 366.

[15] Newman, J. C., Jr.; and Raju, I. S.: Stress-Intensity Factor Equations for Cracks in Three-Dimensional Finite Bodies. Fracture Mechanics: Fourteenth Symposium--Volume I: Theory and Analysis, ASTM STP 791, American Society for Testing and Materials, 1983, pp. I-238-I-268.

TABLE 1--Properties of fiber and matrix or winding resin.

	Helical fiber	Broadgoods fiber	Matrix
Tensile modulus, GPa (Msi)	228 (33)	228 (33)	2.85 (0.414)
Poisson's ratio	...	...	.35
Tensile strength, GPa (ksi)	3.96 (574)	.75 (544)	...
Elongation at failure	0.0167	...	...
Density, kg/m^3 ($lbm/in.^3$)	1790 (0.0648)	1780 (0.0642)	1230

TABLE 2--Physical properties of composite ring.

Property	Value
Composite density, kg/m^3 ($lbm/in.^3$)	1490 (0.0540)
Resin mass fraction	0.346
Resin volume fraction	0.385
Fiber volume fraction	0.545
Void content	0.0706

TABLE 3--Lamina constants.

	Unidirectional broadgoods	Helical layers	Cut helical layers	Cloth
E_{11}, GPa (Msi)	1.06 (15.4)	111 (16.2)	111 (16.2)	59.3 (8.60)
E_{22}, GPa (Msi)	6.39 (0.927)	1.92 (0.278)	1.92 (0.278)	59.3 (8.60)
G_{12}, GPa (Msi)	4.47 (0.649)	4.28 (0.621)	4.28 (0.621)	3.68 (0.533)
ν_{12}	0.275	0.267	0.267	0.0348
Layer thickness, μm (in.)	[a]0.427 (16.8)	0.427 (16.8)	0.711 (28.0)	0.427 (16.8)

[a]Equal to three plies of broadgoods.

TABLE 4--Laminate constants.

Property	Value
E_x, GPa (Msi)	30.6 (4.44)
E_y, GPa (Msi)	39.0 (5.66)
G_{xy}, GPa (Msi)	19.7 (2.86)
ν_{xy}	0.351
ν_{yx}	0.447

TABLE 5--Test results for 12.7—mm—diameter hemisphere, 5.03 kg impacter, and empty ring. Specimens were 38 mm wide.

Specimen number	Kinetic energy, J (ft—lbf)	Max. Impact force, kN (kips)	Damage depth, mm (in.)	Loads, kN (kips) for failure of —	
				First ligament	Remaining ligament
6—1	17.0 (12.5)	19.3 (4.34)	0.8 (0.03)	481 (107)	(a)
6—10		19.9 (4.47)	.8 (.03)	482 (108)	(a)
6—19		19.7 (4.43)	.0	484 (109)	(a)
6—28		19.3 (4.34)	.0	459 (103)	(a)
6—37		19.9 (4.47)	.0	468 (105)	(a)
6—2	33.9 (25.0)	26.2 (5.89)	1.0 (.039)	469 (106)	(a)
6—11		b26.0 (5.85)	2.0 (.079)	462 (104)	(a)
6—20		b28.1 (6.32)	.0	462 (104)	(a)
6—29		b27.7 (6.23)	.5 (.02)	410 (92.2)	439 (98.7)
6—38		b23.0 (5.17)	1.7 (.067)	477 (107)	(a)
6—3	67.8 (50.0)	b34.8 (7.82)	2.7 (.11)	431 (96.9)	453 (102)
6—12		b34.7 (7.80)	2.0 (.080)	409 (91.9)	439 (98.7)
6—21		b29.8 (6.70)	2.5 (.10)	429 (96.4)	434 (97.6)
6—30		b31.5 (7.08)	3.0 (.12)	439 (98.7)	(a)
6—39		b35.9 (8.07)	2.3 (.090)	399 (89.7)	412 (92.6)
6—4	136. (100.)	b45.5 (10.2)	3.9 (.16)	409 (91.9)	400 (89.9)
6—13		b —	3.0 (.12)	392 (88.1)	401 (90.1)
6—22		b41.7 (9.37)	3.0 (.12)	413 (92.8)	(a)
6—31		b41.9 (9.42)	3.2 (.13)	382 (85.9)	417 (93.7)
6—40		b37.8 (8.50)	4.2 (.17)	380 (85.4)	417 (93.7)

a — Catastrophic failure.

b — Impact caused visible crater.

TABLE 6--Test results for 12.7-mm-diameter hemisphere, 5.03 kg impacter, and filled ring. Specimens were 38 mm wide.

Specimen number	Kinetic energy, J (ft-lbf)	Max. impact force, kN (kips)	Damage depth, mm (in.)	Loads, kN (kips) for failure of	
				First ligament	Remaining ligament
1-1	17.0 (12.5)	23.3 (5.24)	0.3 (0.01)	418 (94.0)	(a)
1-10		22.4 (5.04)	.3 (.01)	455 (102)	(a)
1-19		22.0 (4.95)	.0	386 (86.8)	383 (86.1)
1-28		21.7 (4.88)	.0	416 (93.5)	394 (88.6)
1-37		24.1 (5.42)	.0	458 (103)	(a)
1-2	33.9 (25.0)	b31.8 (7.15)	1.1 (.045)	398 (89.5)	419 (94.2)
1-11		b32.8 (7.37)	1.5 (.060)	379 (85.2)	417 (93.7)
1-20		b29.6 (6.65)	2.4 (.095)	427 (96.0)	443 (99.6)
1-29		b31.5 (7.08)	.8 (.03)	393 (88.3)	407 (91.5)
1-38		b30.9 (6.95)	.8 (.03)	416 (93.5)	(a)
1-3	67.8 (50.0)	b40.9 (9.19)	3.0 (.12)	339 (76.2)	385 (86.6)
1-12		b41.1 (9.24)	2.0 (.080)	400 (89.9)	435 (97.8)
1-21		b36.3 (8.16)	2.7 (.11)	379 (85.2)	460 (103)
1-30		b43.2 (9.71)	3.3 (.13)	359 (80.7)	395 (88.8)
1-39		b35.3 (7.94)	3.3 (.13)	385 (86.6)	405 (91.0)
1-4	136. (100.)	b58.0 (13.0)	3.2 (.13)	334 (75.1)	374 (84.1)
1-13		b52.4 (11.8)	4.2 (.17)	334 (75.1)	391 (87.9)
1-22		b54.9 (12.3)	3.7 (.15)	366 (82.3)	403 (90.6)
1-31		b -	3.4 (.14)	354 (79.6)	408 (91.7)
1-40		b52.7 (11.8)	4.1 (.16)	346 (77.8)	395 (88.8)

a - Catastrophic failure.

b - Impact caused visible crater.

TABLE6.AST

TABLE 7--Test results for corner, 5.26 kg impacter, and empty ring. Specimens were 38 mm wide. All impacts caused a visible crater.

Specimen number	Kinetic energy, J (ft-lbf)	Max. impact force, kN (kips)	Damage depth, mm (in.)	Loads, kN (kips) for failure of —	
				First ligament	Remaining ligament
6-6	17.0 (12.5)	10.3 (2.32)	3.7 (0.075)	444 (99.8)	(a)
6-15		11.1 (2.50)	2.2 (.085)	461 (104)	(a)
6-24		—	2.2 (.085)	485 (109)	(a)
6-33		10.9 (2.45)	2.0 (.080)	463 (104)	(a)
6-41		10.5 (2.36)	2.0 (.080)	b485 (109)	(a)
6-7	33.9 (25.0)	14.9 (3.35)	2.7 (.11)	427 (96.0)	(a)
6-16		18.9 (4.25)	2.7 (.11)	480 (108)	(a)
6-25		16.4 (3.69)	2.9 (.12)	441 (99.1)	(a)
6-34		17.2 (3.87)	2.7 (.11)	456 (103)	(a)
6-42		15.1 (3.39)	2.5 (.10)	474 (107)	(a)
6-8	67.8 (50.0)	23.1 (5.19)	3.7 (.15)	412 (92.6)	(a)
6-17		26.5 (5.96)	3.7 (.15)	419 (94.2)	(a)
6-26		25.8 (5.80)	3.2 (.13)	407 (91.5)	(a)
6-35		25.4 (5.71)	3.8 (.15)	405 (91.0)	387 (87.0)
6-43		23.5 (5.28)	3.3 (.13)	414 (93.1)	(a)
6-9	136. (100.)	37.3 (8.39)	5.0 (.20)	355 (79.8)	404 (90.8)
6-18		37.0 (8.32)	5.6 (.22)	378 (85.0)	410 (92.2)
6-27		42.3 (9.51)	4.3 (.17)	376 (84.5)	423 (95.1)
6-36		40.0 (8.99)	4.6 (.18)	383 (86.1)	428 (96.2)
6-44		38.6 (8.68)	4.4 (.18)	—	—

a — Catastrophic failure.

b — No failure.

TABLE 8--Test results for corner, 5.26 kg impacter, and filled ring. Specimens were 38 mm wide. All impacts caused a visible crater.

Specimen number	Kinetic energy, J (ft-lbf)	Max. impact force, kN (kips)	Damage depth, mm (in.)	Loads, kN (kips) for failure of -	
				First ligament	Remaining ligament
1-6	17.0 (12.5)	13.1 (2.94)	2.7 (0.11)	383 (86.1)	(a)
1-17		12.5 (2.81)	2.7 (.11)	364 (81.8)	385 (86.6)
1-24		11.2 (2.52)	-	-	-
1-33		-	3.0 (.12)	440 (98.9)	(a)
1-41		11.8 (2.65)	2.5 (.10)	433 (97.3)	(a)
1-7	33.9 (25.0)	18.3 (4.11)	2.9 (.11)	381 (85.7)	419 (94.2)
1-16		20.3 (4.56)	3.0 (.12)	397 (89.2)	(a)
1-25		18.6 (4.18)	2.9 (.12)	429 (96.4)	(a)
1-34		19.2 (4.32)	-	-	-
1-42		19.9 (4.47)	3.2 (.13)	400 (89.9)	408 (91.7)
1-8	67.8 (50.0)	28.1 (6.32)	4.2 (.17)	326 (73.3)	399 (89.7)
1-15		28.6 (6.43)	3.7 (.15)	402 (90.4)	(a)
1-26		29.9 (6.72)	4.1 (.16)	384 (86.3)	387 (87.0)
1-35		27.9 (6.27)	4.2 (.17)	374 (84.1)	397 (89.2)
1-43		28.8 (6.47)	3.8 (.15)	394 (88.6)	(a)
1-9	136. (100.)	43.5 (9.78)	5.7 (.23)	369 (83.0)	427 (96.0)
1-18		40.9 (9.19)	5.2 (.21)	342 (76.9)	422 (94.9)
1-27		47.4 (10.7)	5.2 (.21)	327 (73.5)	375 (84.3)
1-36		46.3 (10.4)	5.7 (.23)	351 (78.9)	440 (98.9)
1-5		46.4 (10.4)	5.5 (.22)	319 (71.7)	417 (93.7)
1-44		-	5.1 (.20)	317 (71.3)	394 (88.6)

a - Catastrophic failure.

TABLE 9--Test results for 6.35-mm-diameter rod impacter. Impacts were simulated. Specimens were 38 mm wide.

Specimen number	Work, J (ft-lbf) (a)	Stroke, mm (in.) (b)	Max. contact force, kN (kips)	Damage depth, mm (in.)	Loads, kN (kips) for failure of	
					First ligament	Remaining ligament
4-41	64.8 (47.8)	3.3 (0.13)	30.1 (6.77)	5.0 (0.20)	386 (86.8)	398 (89.5)
6-14	72.0 (53.1)		29.1 (6.54)	4.8 (.19)	367 (82.5)	402 (90.4)
1-23	66.8 (49.3)		30.2 (6.79)	5.6 (.22)	412 (92.6)	417 (93.7)
4-43	163 (120)	6.6 (.26)	32.2 (7.24)	8.0 (.31)	277 (51.0)	397 (89.2)
1-32	183 (135)		35.8 (8.05)	8.0 (.31)	270 (60.7)	412 (92.6)
6-23	163 (120)		34.0 (7.64)	8.4 (.33)	282 (63.4)	409 (91.9)
6-32	276 (204)	9.4 (.37)	39.1 (8.79)	9.1 (.36)	266 (59.8)	433 (97.3)
4-44	273 (201)		40.5 (9.10)	10.3 (.41)	311 (69.9)	342 (76.9)
2-6	289 (213)		39.6 (8.90)	8.6 (.34)	305 (68.6)	405 (91.0)

a - Area under load stroke curve.

b - Displacement of rod.

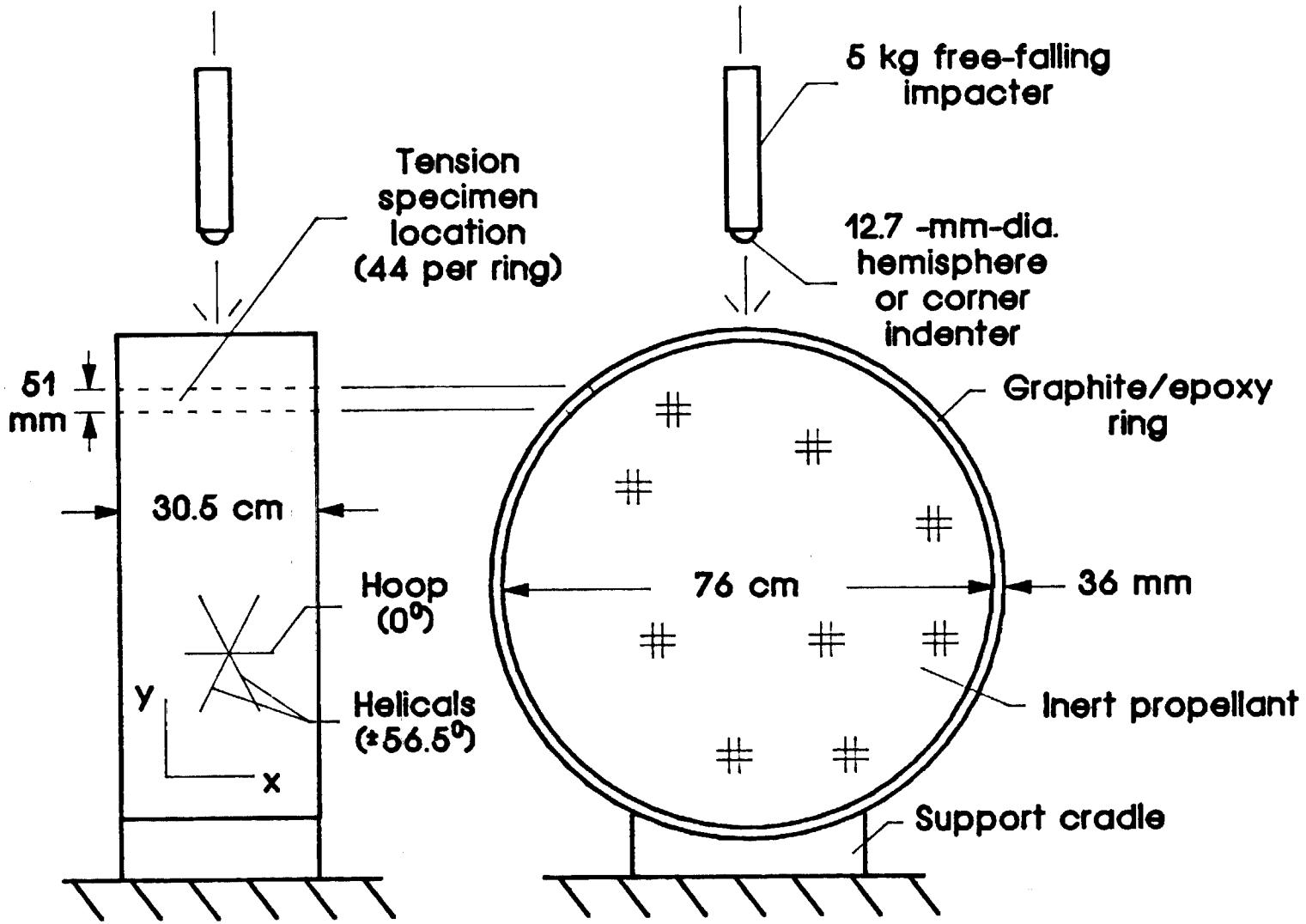

Figure 1.- Impact tests of FWC-like ring.

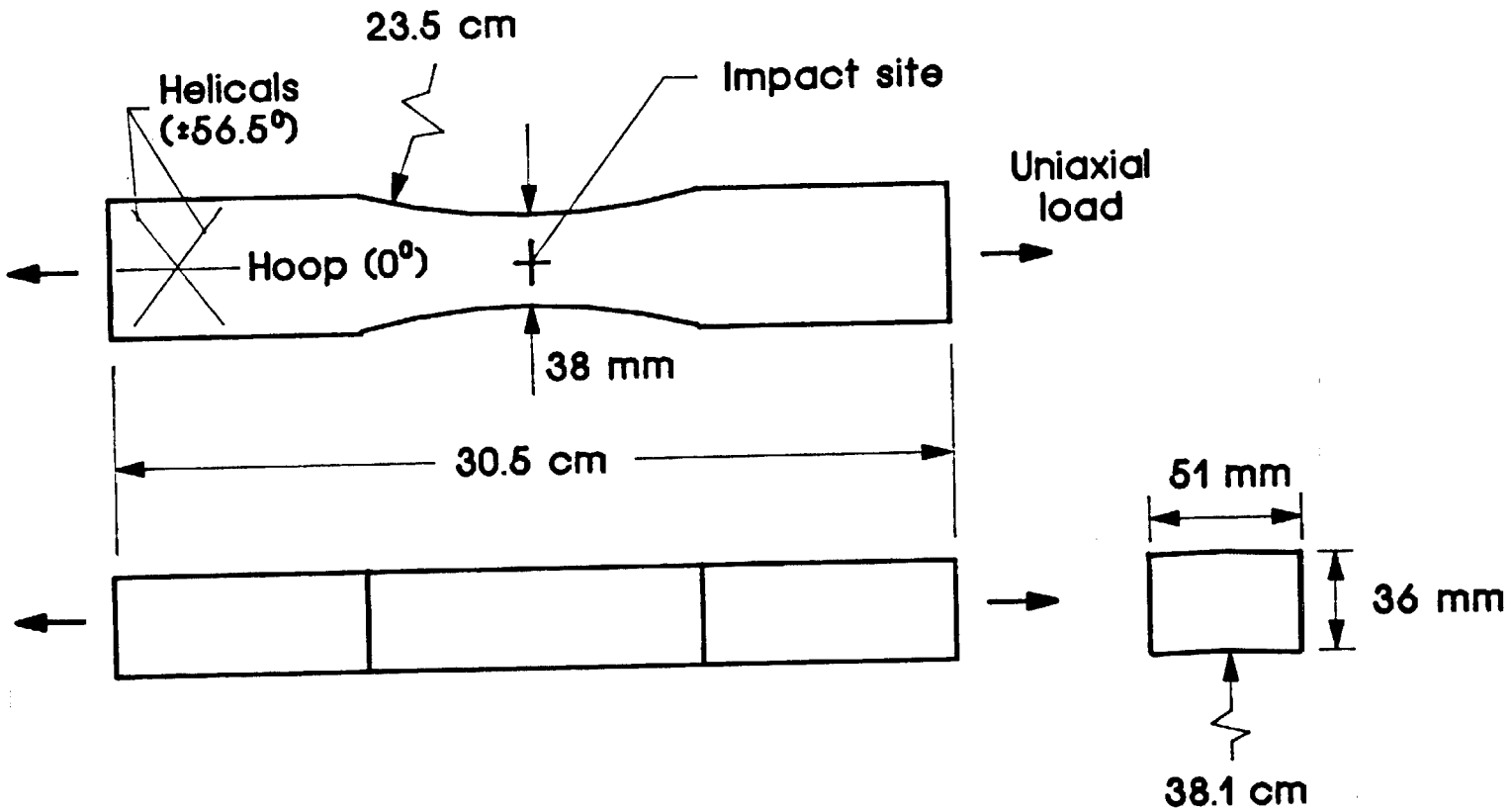

Figure 2.- Tension specimen used to measure residual strength.

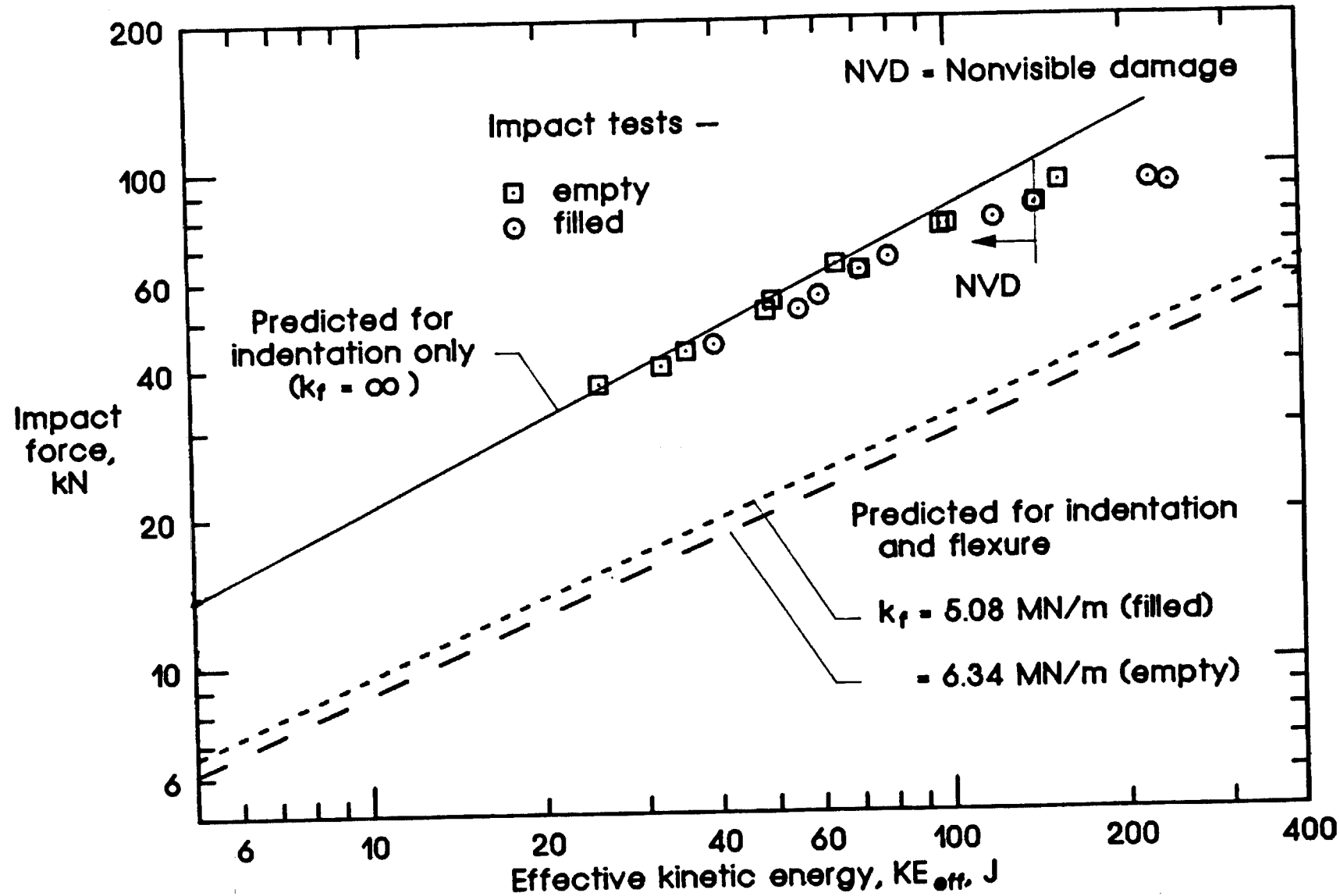

Figure 3.- Impact force versus effective kinetic energy for 25.4-mm- (1.0-in.) diameter hemisphere.

\IMPACT89\FG3.AST

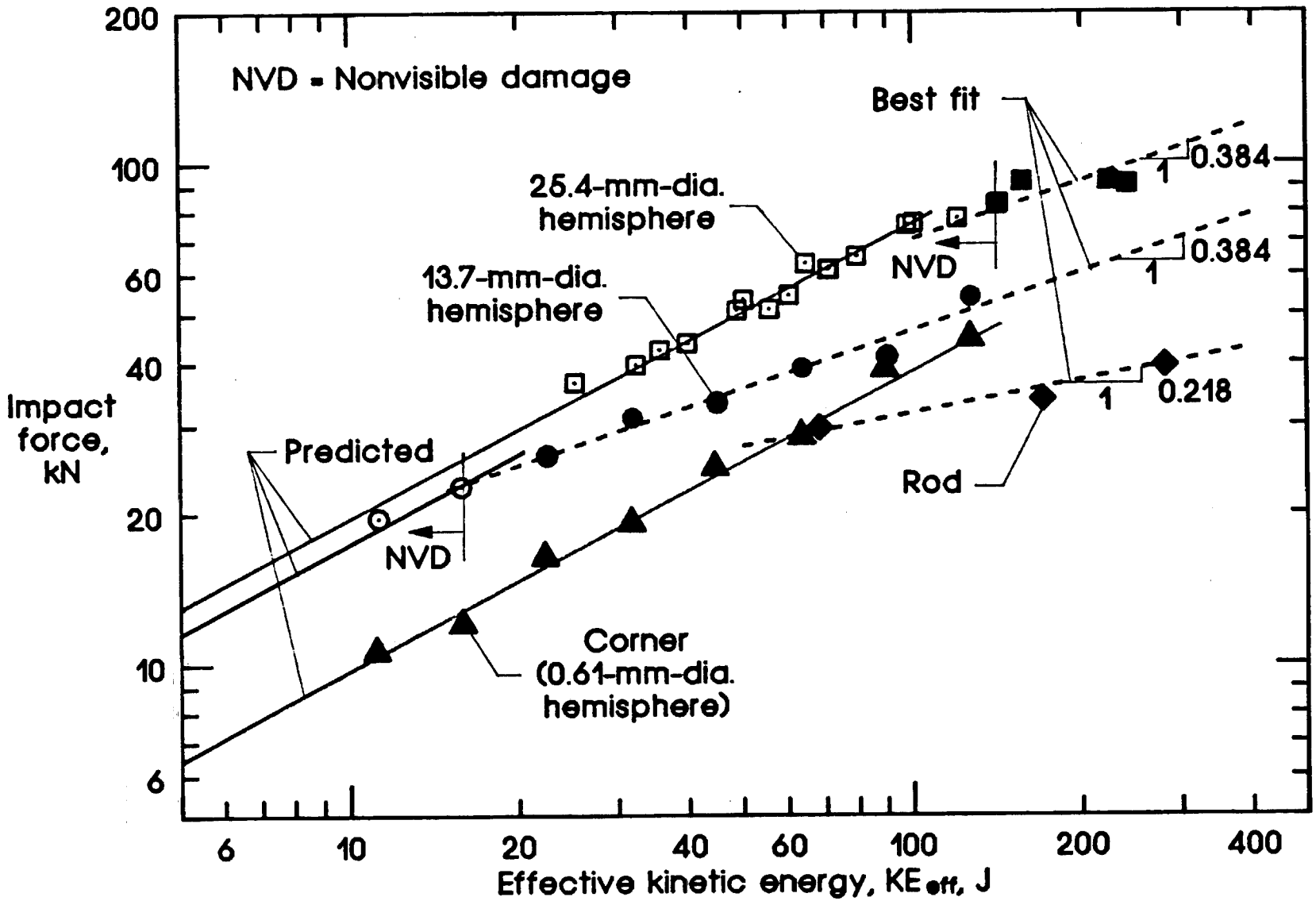

Figure 4.- Effect of impacter shape on impact force.

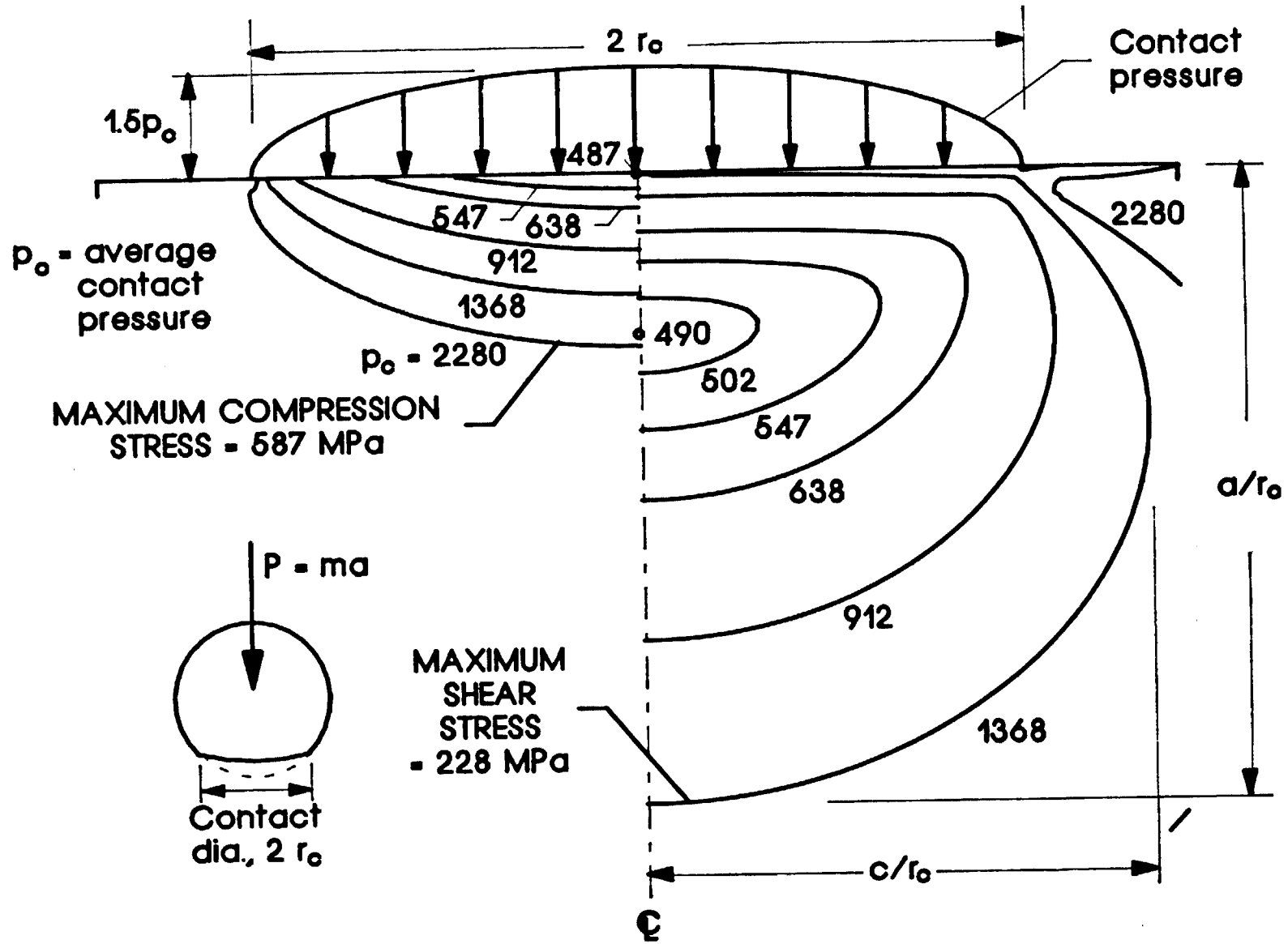

Figure 5.- Damage contours from isotropic, theory of elasticity according to A. E. H. Love.

\IMPACT89\RG5.AST

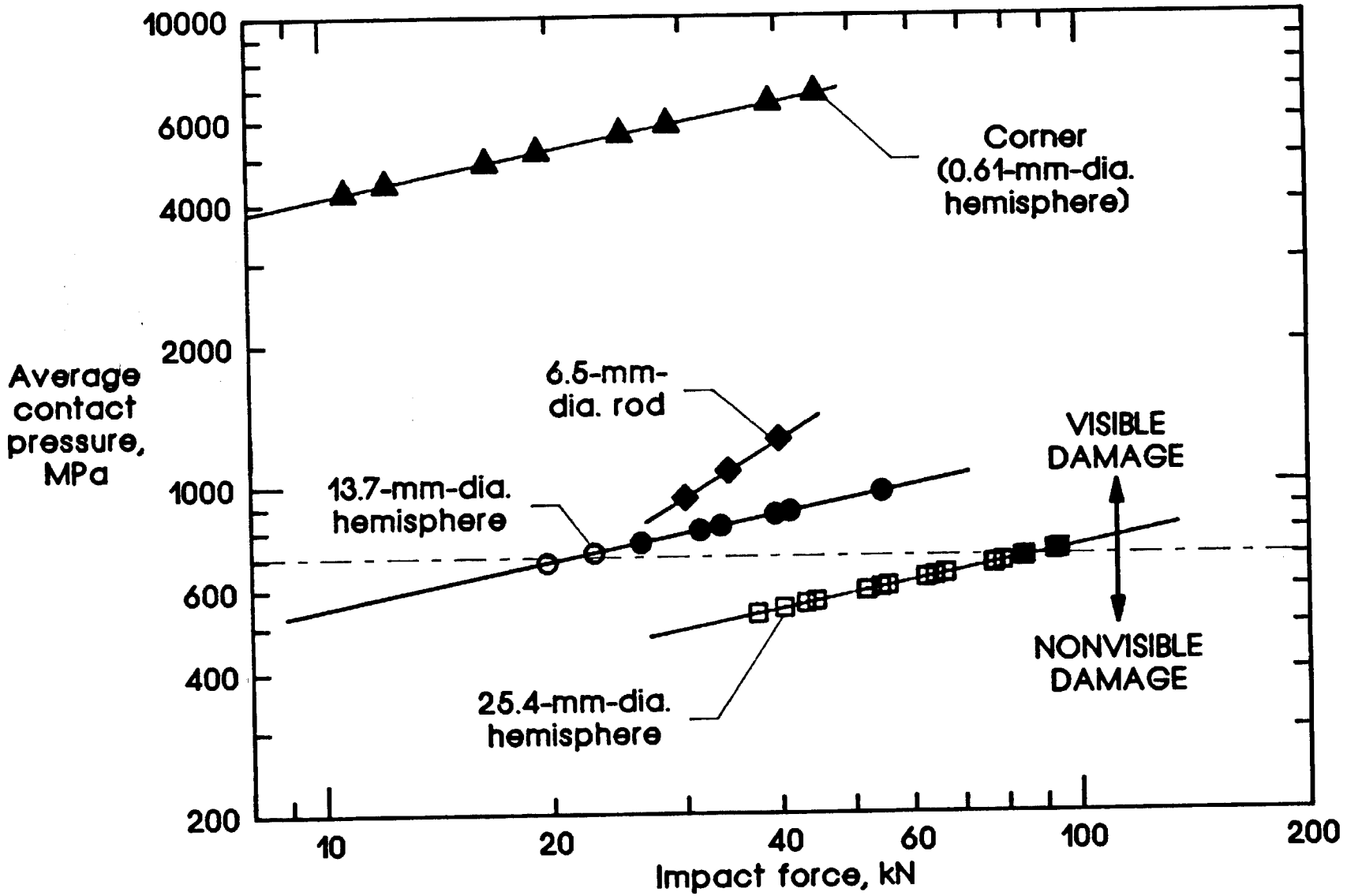

Figure 6.- Effect of impacter shape on contact pressure.

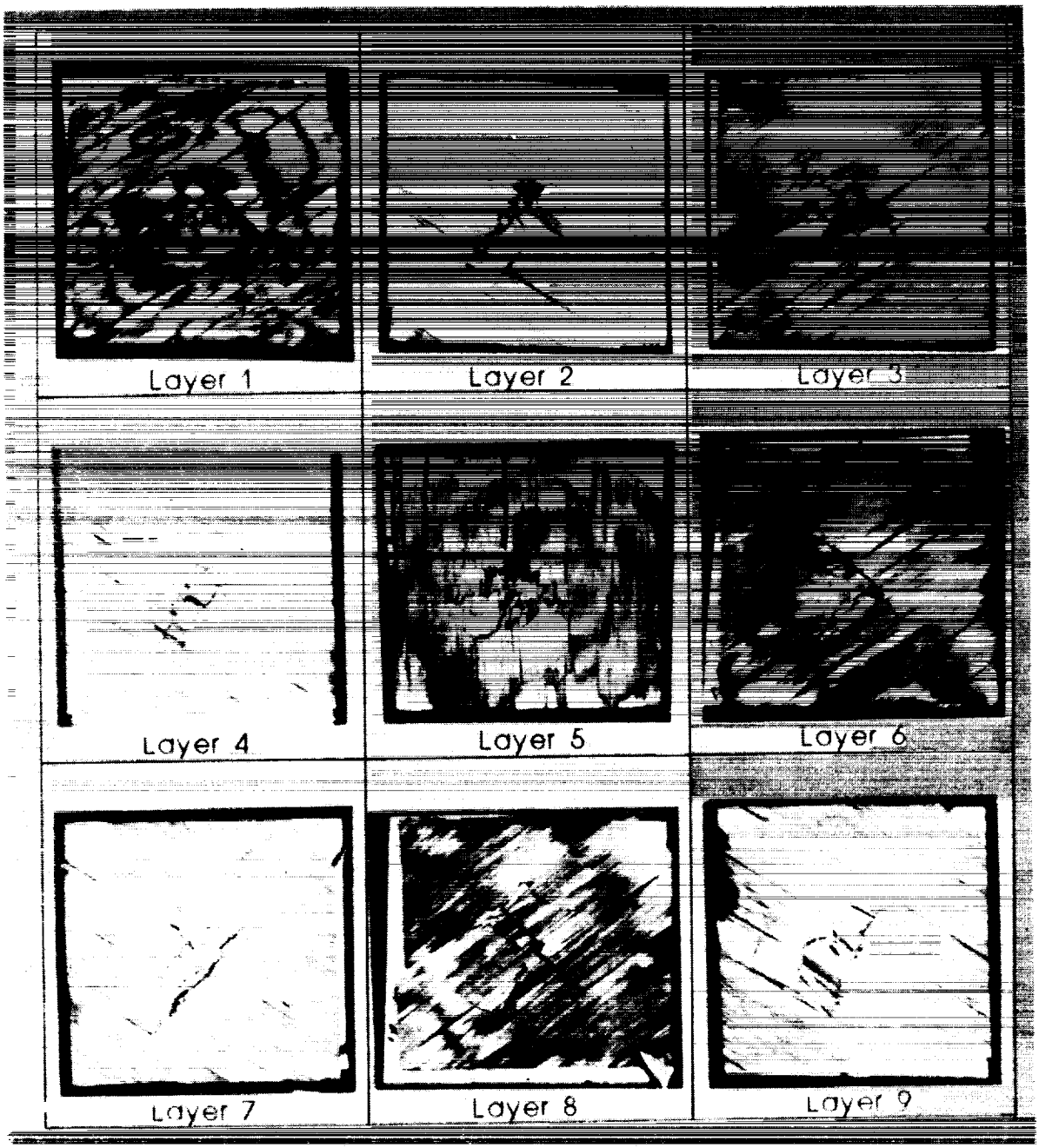

Figure 7. Damaged layers from deplied specimen with simulated impact (50.8-mm-dia. indenter and 267-kN contact force).

\IMPACT89\FIG7.AST

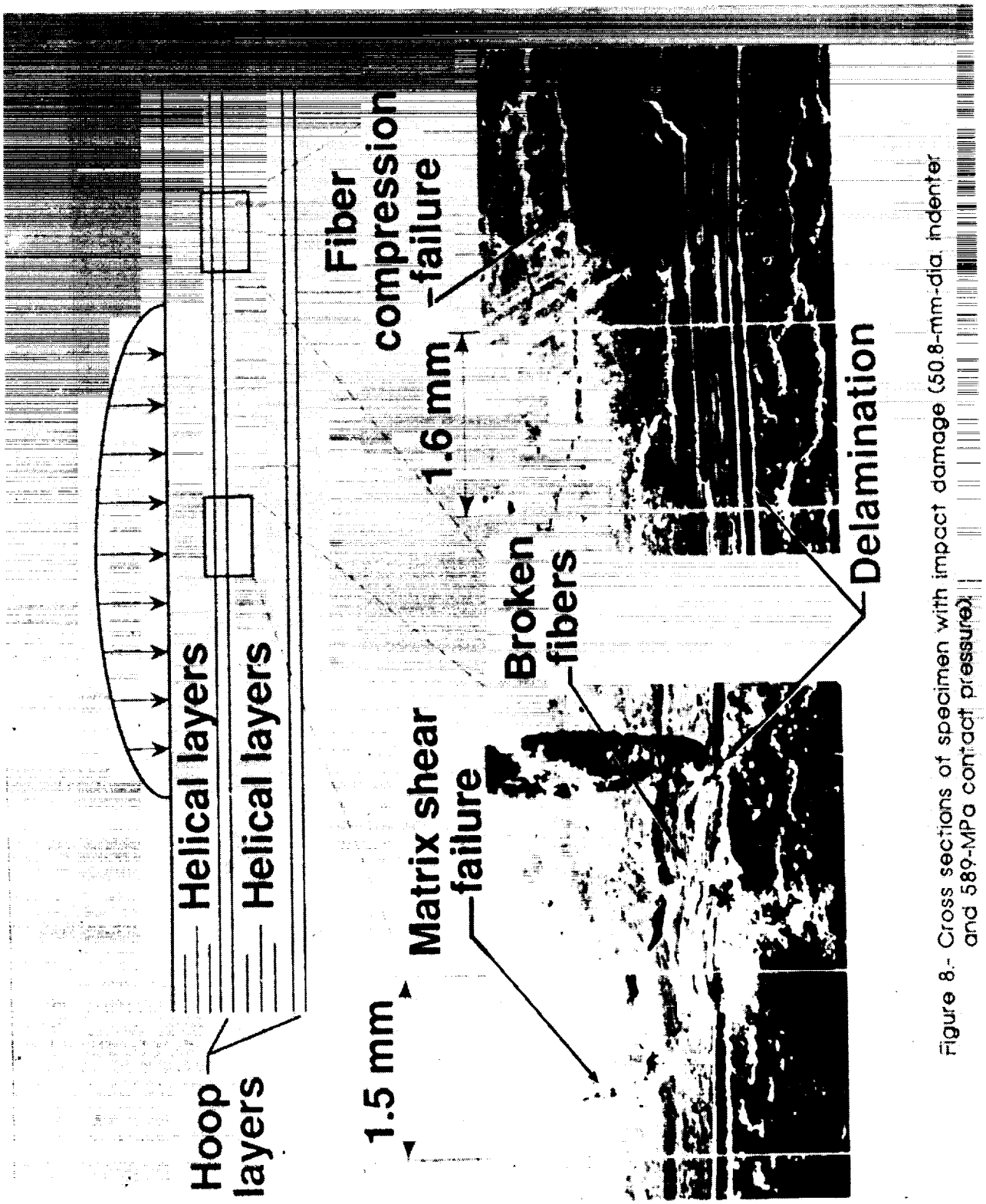

Figure 8.- Cross sections of specimen with impact damage (50.8-mm-dia. indenter and 589-MPa contact pressure).

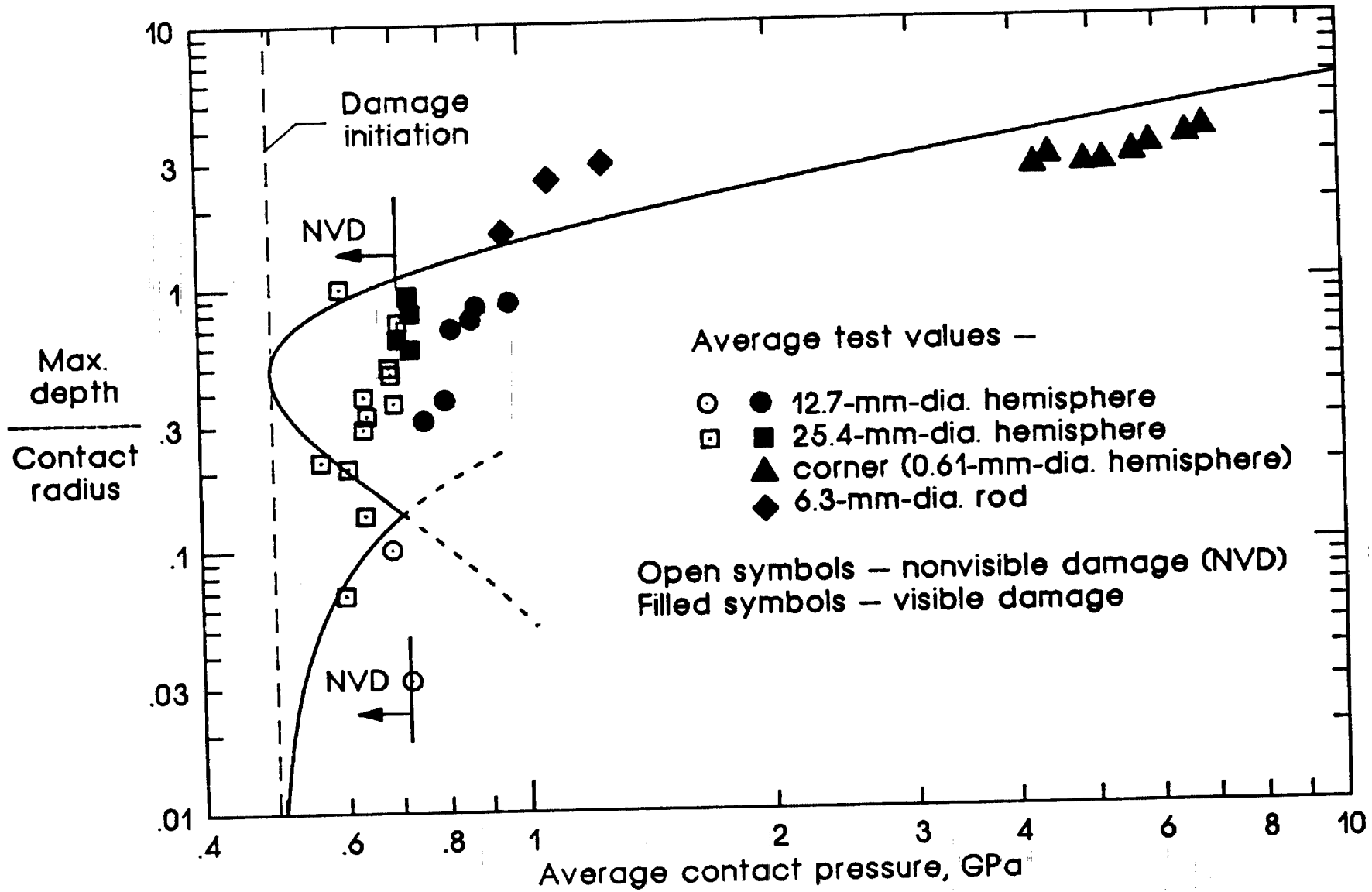

Figure 10.- Effect of impacter shape on damage depth. Depths were measured in radiographs.

\IMPACT89\FIG10.AST

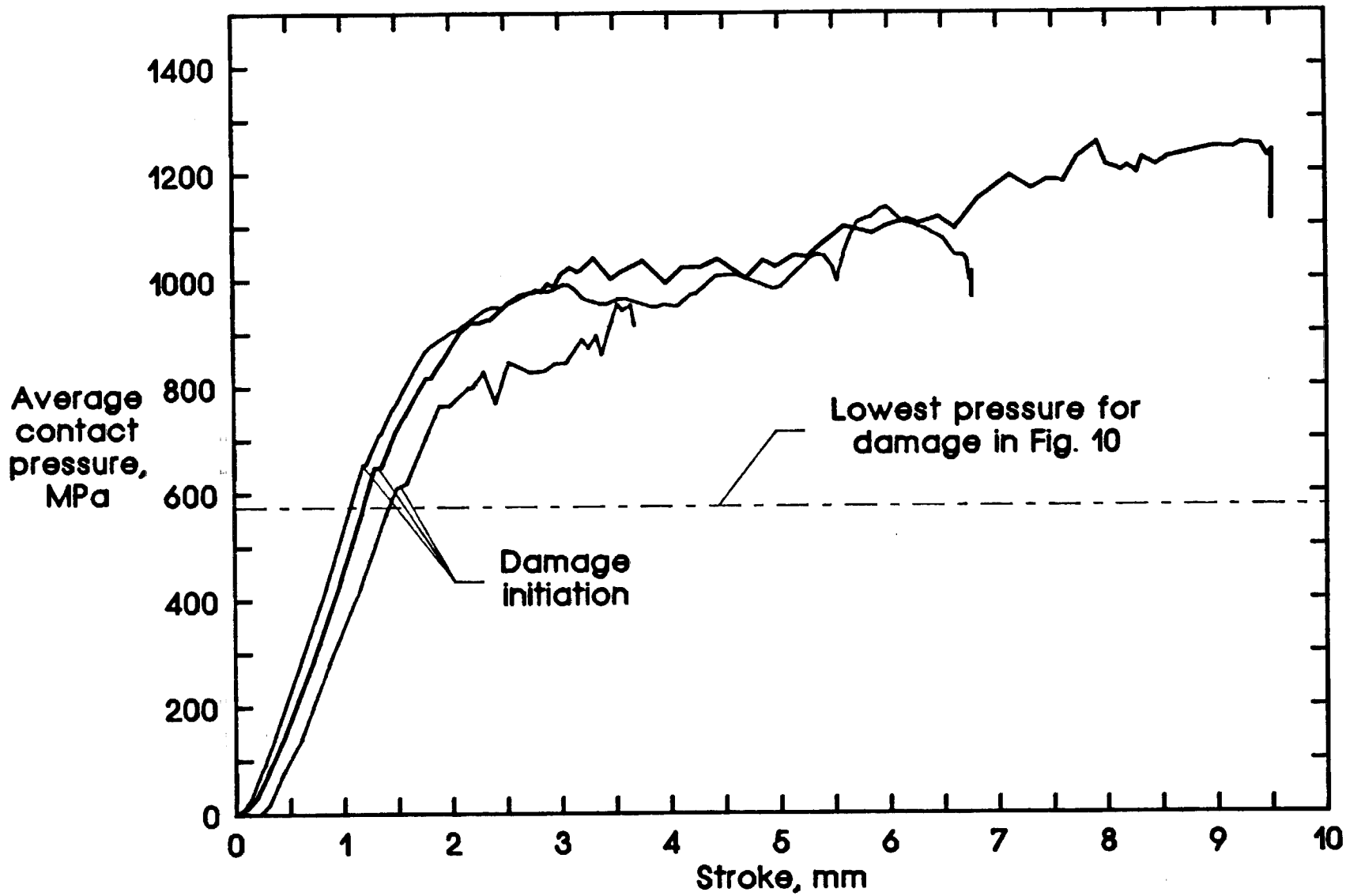

Figure 11.- Contact pressure versus stroke for the 6.3-mm-dia. (.25-in.) rod indenter -- three tests.

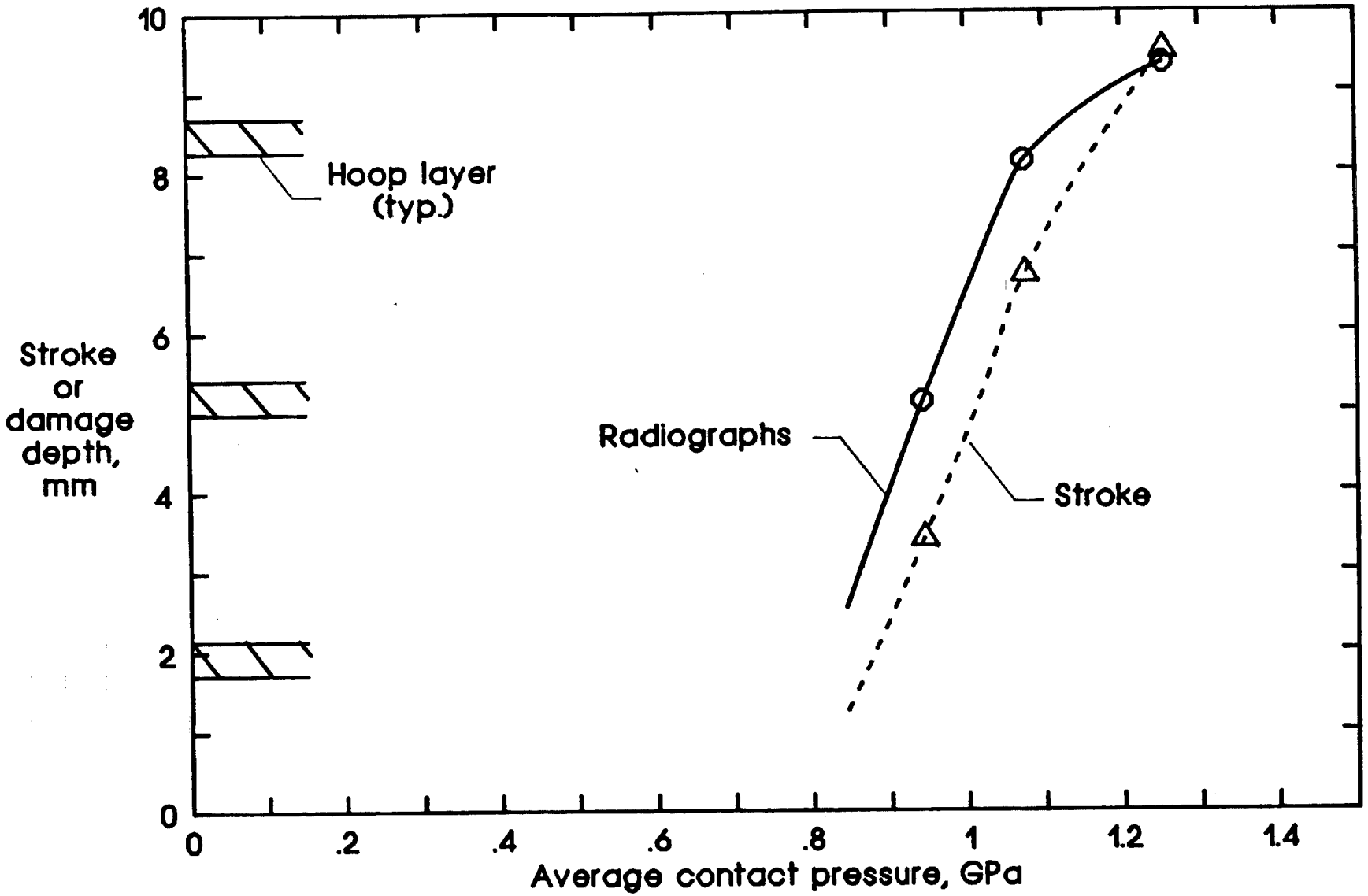

Figure 12.- Comparison between radiographs and stroke for 6.4-mm- (0.25-in.) diameter rod indenter.

\IMPACT89\FIG12.AST

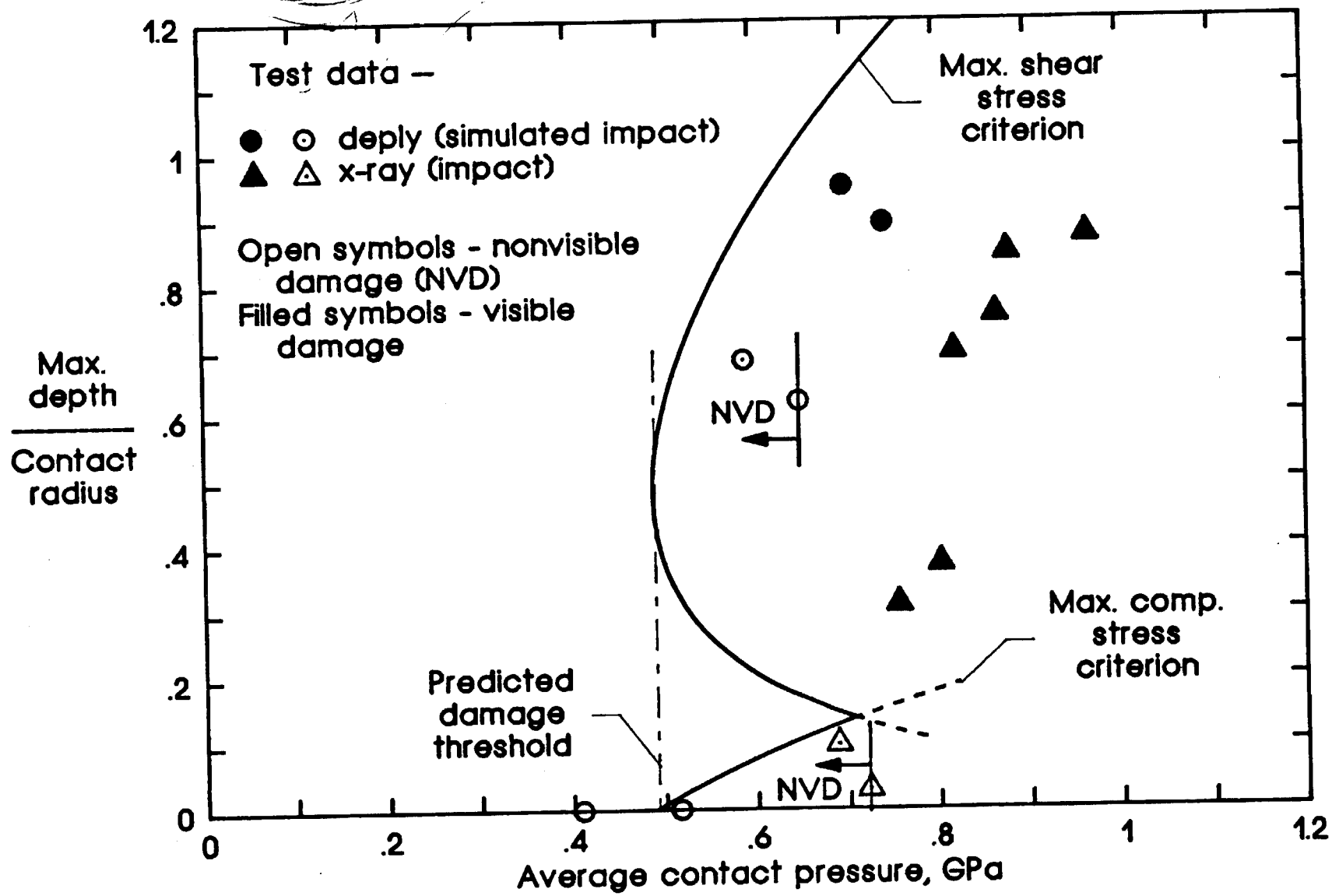

Figure 13.- Comparison of damage depth from deply and raiographs for 12.7-mm-dia. hemisphere.

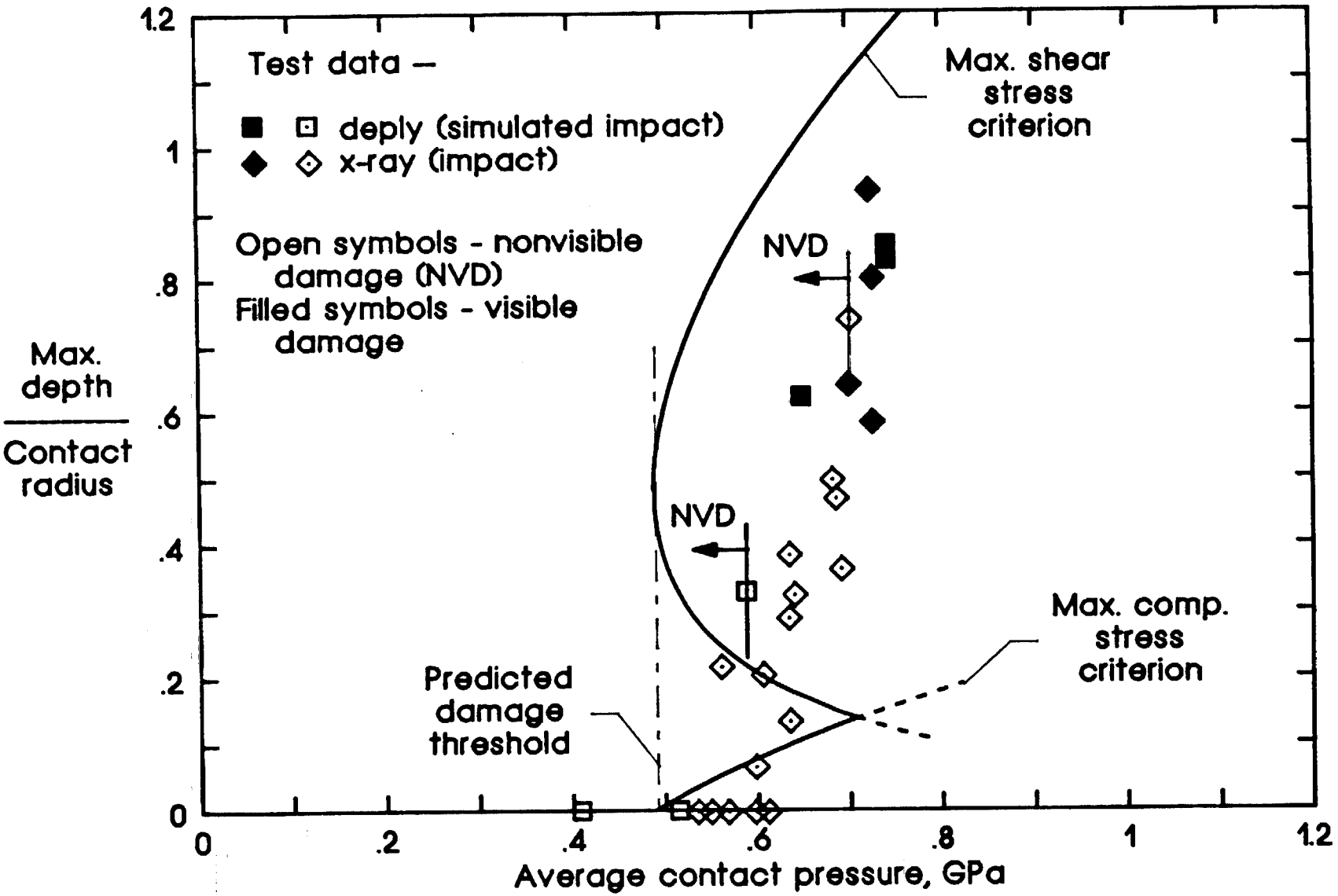

Figure 14.- Comparison of damage depth from deply and raiographs for 25.4-mm-dia. hemisphere.

\IMPACT89\FIG14.AST

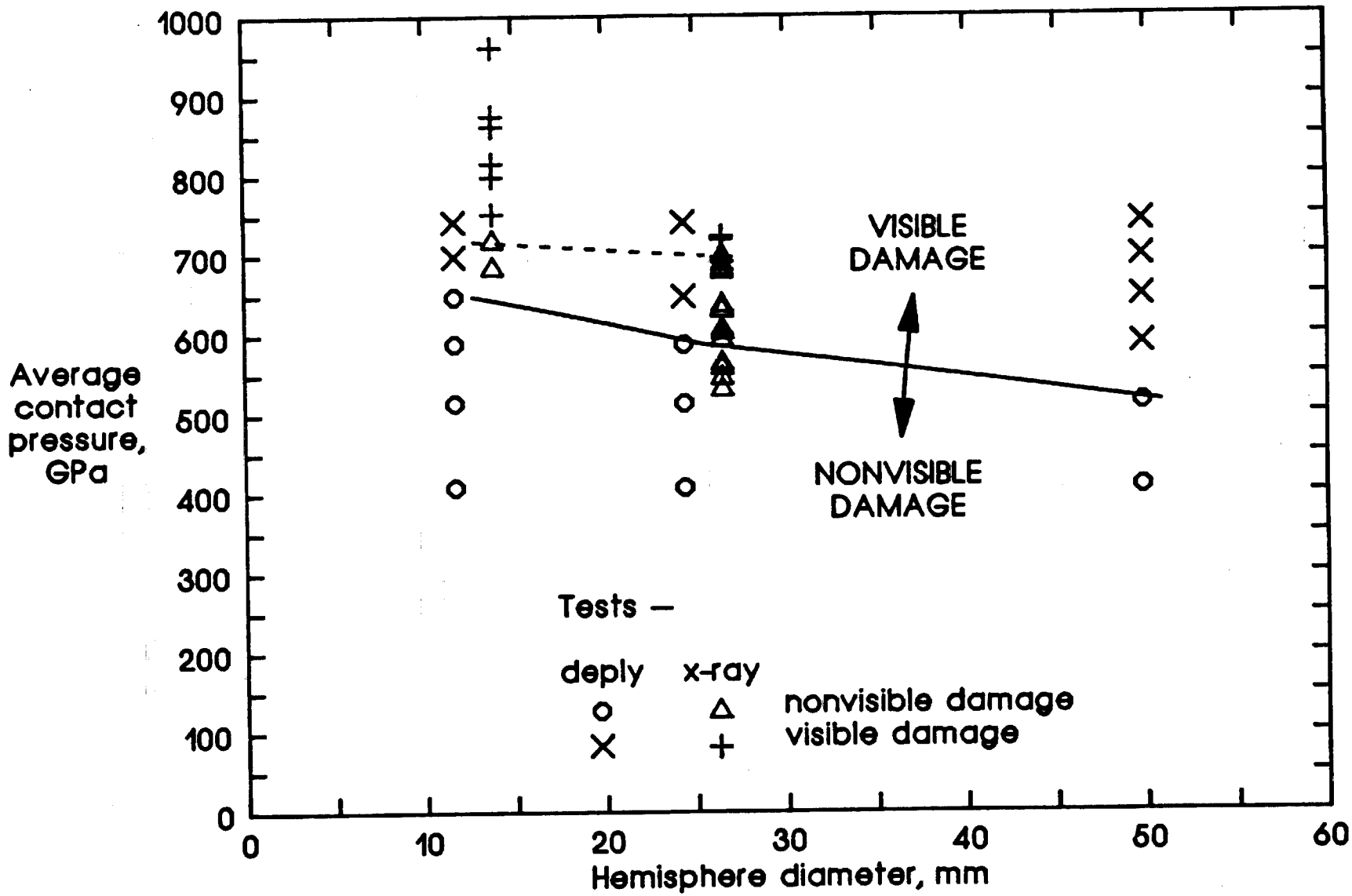

Figure 15.- Effect of hemisphere diameter on visibility of damage depth.

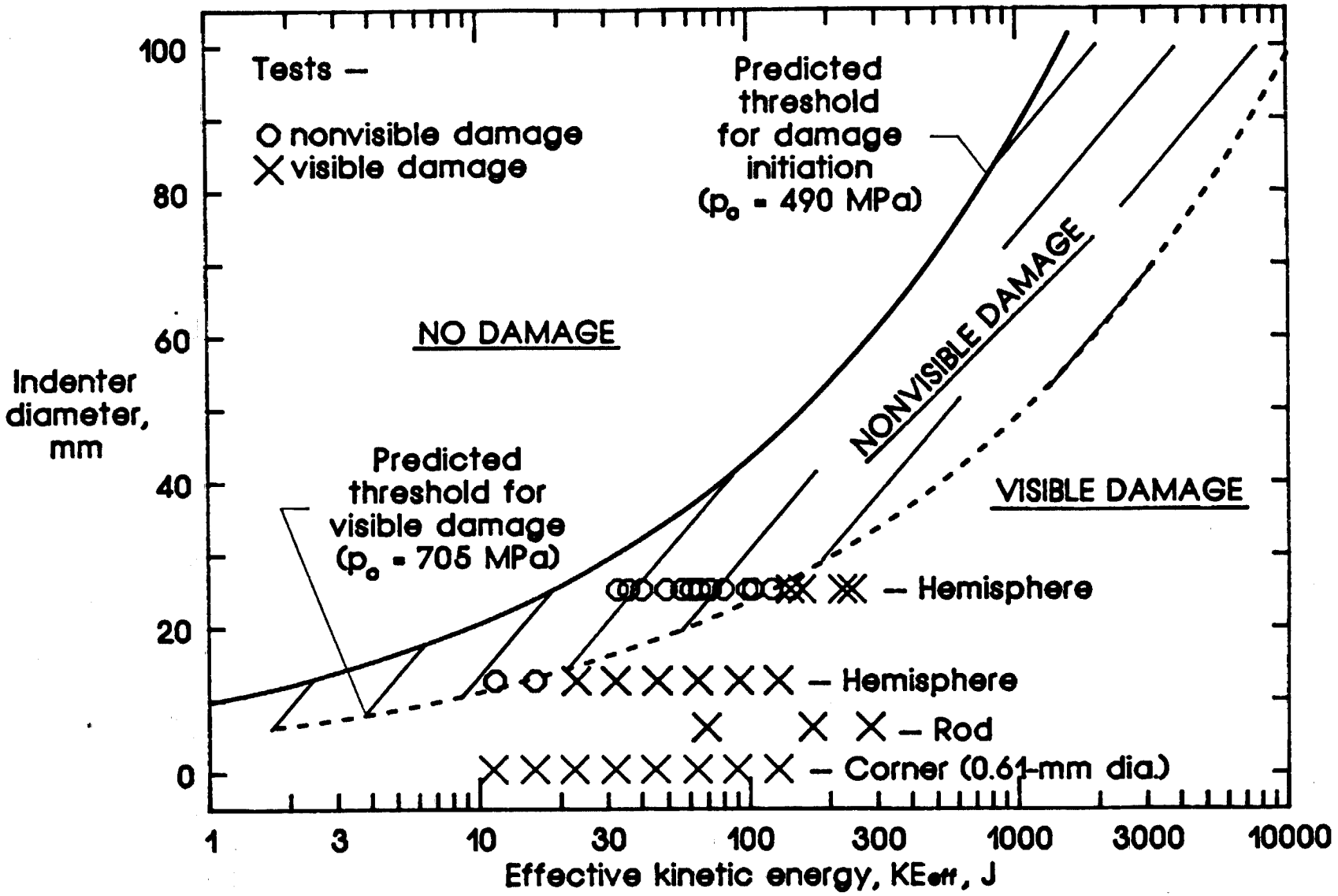

Figure 16.- Indenter diameter and effective kinetic energy to cause damage.

\IMPACT89\FIG16.AST

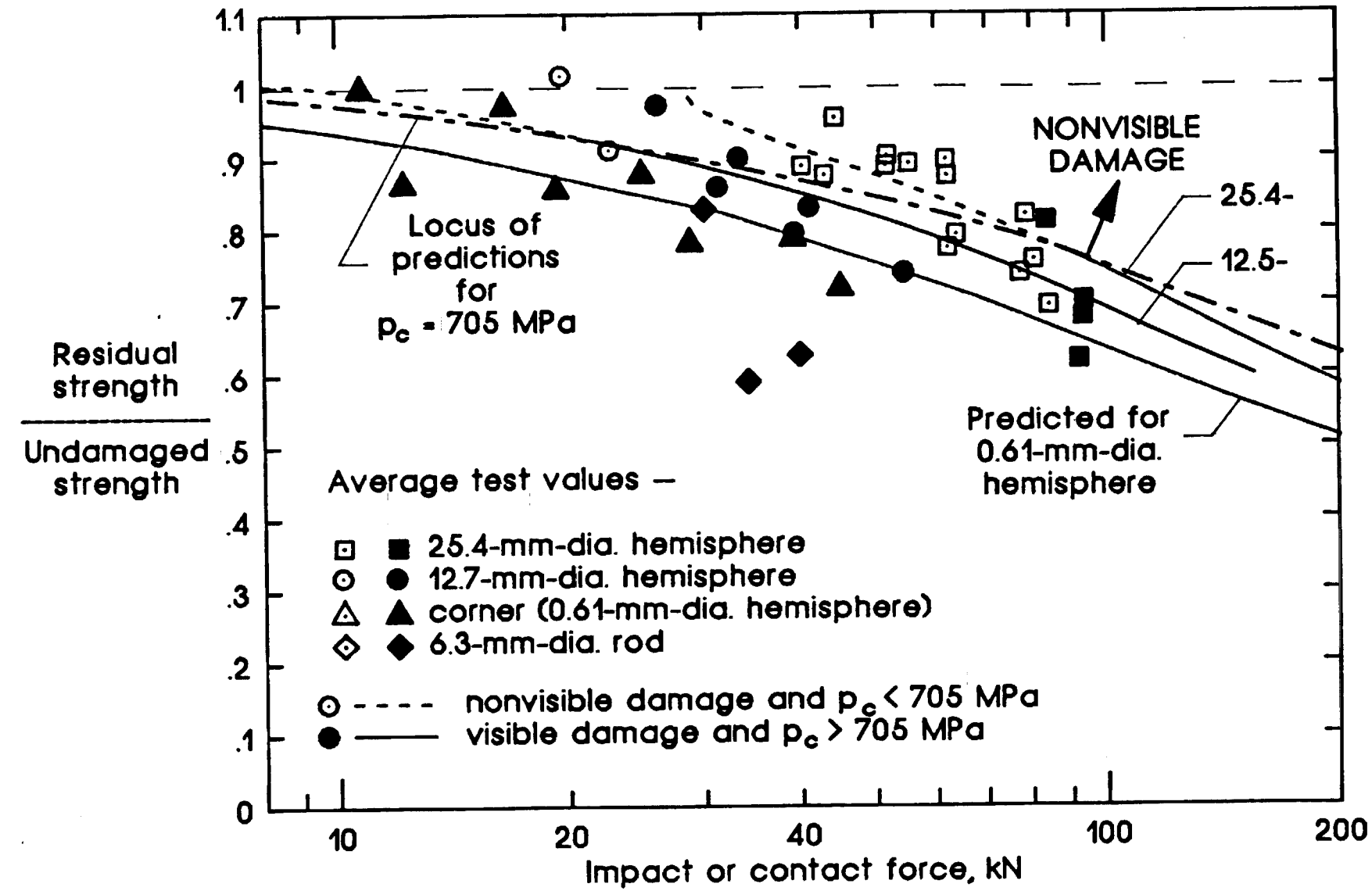

Figure 17.- Effect of indenter shape on first-ligament strength.

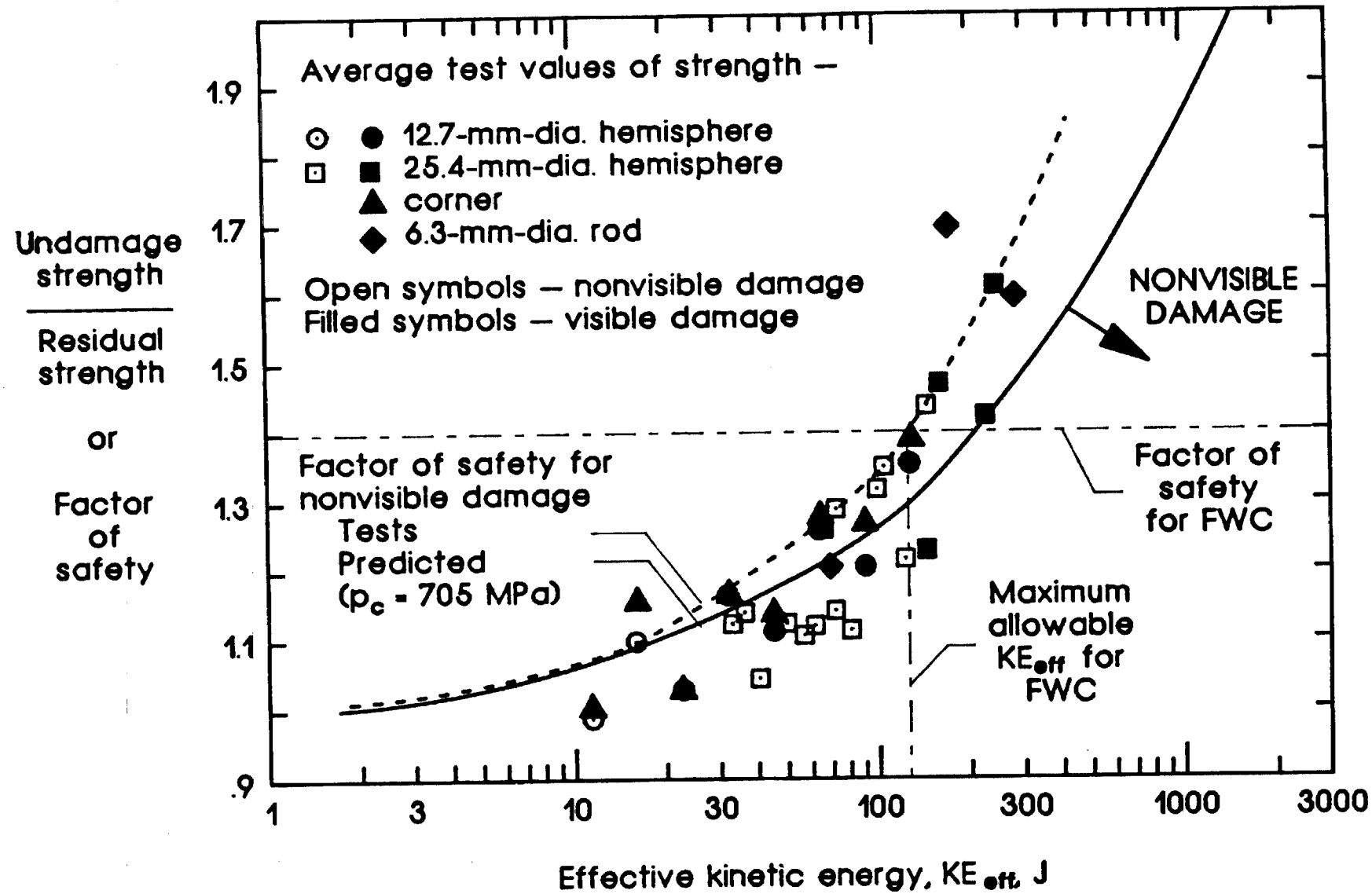

Figure 18.- Factor of safety for nonvisible damage versus effective kinetic energy.

\IMPACT89\FIG18.AST

NASA
National Aeronautics and Space Administration

Report Documentation Page

1. Report No.	2. Government Accession No.	3. Recipient's Catalog No.
NASA TM-102599		

4. Title and Subtitle
Relevance of Impacter Shape to Nonvisible Damage and Residual Tensile Strength of a Thick Graphite/Epoxy Laminate

5. Report Date
January 1990

6. Performing Organization Code

7. Author(s)
C. C. Poe, Jr.

8. Performing Organization Report No.

10. Work Unit No.
505-63-01-05

9. Performing Organization Name and Address
NASA Langley Research Center
Hampton, VA 23665-5225

11. Contract or Grant No.

13. Type of Report and Period Covered
Technical Memorandum

12. Sponsoring Agency Name and Address
National Aeronautics and Space Administration
Washington, DC 20546-0001

14. Sponsoring Agency Code

15. Supplementary Notes
This paper was presented at the ASTM Third Symposium on Composite Materials: Fatigue and Fracture. Orlando, Florida, November 6-9, 1989.

16. Abstract

A study was made to determine the relevance of impacter shape to nonvisible damage and tensile residual strength of a 36-mm- (1.4-in.) thick graphite/epoxy motor case. The shapes of the impacters were as follows: 12.7-mm- (0.5-in.) and 25.4-mm- (1.0-in.) diameter hemispheres, a sharp corner, and a 6.3-mm- (0.25-in.) diameter bolt-like rod. The investigation revealed that damage initiated when the contact pressure exceeded a critical level. However, the damage was not visible on the surface until an even higher pressure was exceeded. The damage on the surface consisted of a crater shaped like the impacter, and the damage below the surface consisted of broken fibers. The impact energy to initiate damage or cause visible damage on the surface increased approximately with impacter diameter to the third power. The reduction in strength for nonvisible damage increased with increasing diameter, 9 and 30 percent for the 12.7-mm- (0.5-in.) and 25.4-mm- (1.0-in.) diameter hemispheres, respectively. The corner impacter made visible damage on the surface for even the smallest impact energy. The rod impacter acted like a punch and sliced through the composite. Even so, the critical level of pressure to initiate damage was the same for the rod and hemispherical impacters. Factors of safety for nonvisible damage increased with increasing kinetic energy of impact. The effects of impacter shape on impact force, damage size, damage visibility, and residual tensile strength were predicted quite well assuming Hertzian contact and using maximum stress criteria and a surface crack analysis.

17. Key Words (Suggested by Author(s))	18. Distribution Statement
Low-velocity impact Nonvisible impact damage Impacter shape Residual tension strength Graphite/epoxy composite Motor case	Unclassified - Unlimited Subject Category - 24

19. Security Classif. (of this report)	20. Security Classif. (of this page)	21. No. of pages	22. Price
Unclassified	Unclassified	49	A03

NASA FORM 1626 OCT 86